The structure of Chariklo's rings from stellar occultations

D. Bérard[1], B. Sicardy[1],

J. I. B. Camargo[24,25], J. Desmars[1], F. Braga-Ribas[27,24,25],

J.-L. Ortiz[3], R. Duffard[3], N. Morales[3],

E. Meza[1], R. Leiva[1,6],

G. Benedetti-Rossi[24,25], R. Vieira-Martins[4,23,24,25], A.-R. Gomes Júnior[23], M. Assafin[23],

F. Colas[4], J.-L. Dauvergne[41], P. Kervella[1,26], J. Lecacheux[1], L. Maquet[4], F. Vachier[4], S. Renner[51], B. Monard[52],

A. A. Sickafoose[35,36], H. Breytenbach[35,49], A. Genade[35,49]

W. Beisker[10,44], K.-L. Bath[10,44], H.-J. Bode[10,44,][1], M. Backes[50]

V. D. Ivanov[14,15], E. Jehin[5], M. Gillon[5] J. Manfroid[5] J. Pollock[7], G. Tancredi[20], S. Roland[19], R. Salvo[19], L. Vanzi[2],

D. Herald[11,12,18], D. Gault[11,17], S. Kerr[11,28], H. Pavlov[11,12], K. M. Hill[29], J. Bradshaw[12,13], M. A. Barry[11,30], A. Cool[33,34], B. Lade[32,33,34], A. Cole[29], J. Broughton[11], J. Newman[18], R. Horvat[17], D. Maybour[31], D. Giles[17,31], L. Davis[17], R.A. Paton[17],

B. Loader[11,12], A. Pennell[11,48], P.-D. Jaquiery[47,48],

S. Brillant[15], F. Selman[15], C. Dumas[53], C. Herrera[15], G. Carraro[43], L. Monaco[40], A. Maury[21],

A. Peyrot[42], J.-P. Teng-Chuen-Yu[42],

A. Richichi[46], P. Irawati[37],

C. De Witt[10], P. Schoenau[10], R. Prager[44],

C. Colazo[8,9], R. Melia[9], J. Spagnotto[22], A. Blain[39],

S. Alonso[16], A. Román[38], P. Santos-Sanz[3], J.-L. Rizos[3], J.-L. Maestre[45],

D. Dunham[12]

[1] LESIA, Observatoire de Paris, PSL Research University, CNRS, Sorbonne Universités, UPMC Univ. Paris 06, Univ. Paris Diderot, Sorbonne Paris Cité

[2] Department of Electrical Engineering and Center of Astro-Engineering, Pontificia Universidad Católica de Chile, Av. Vicuña Mackenna 4860, Santiago, Chile

[3] Instituto de Astrofísica de Andalucía, CSIC, Apt. 3004,18080 Granada, Spain

[4] IMCCE, Observatoire de Paris, PSL Research University, CNRS, Sorbonne Universits, UPMC Univ. Paris 06, 77 av. Denfert-Rochereau, 75014, Paris, France

[5] Institut d'Astrophysique de l'Université de Liège, Allée du 6 Août 17, B-4000 Liège, Belgique

[6] Instituto de Astrofísica, Facultad de Física, Pontificia Universidad Católica de Chile, Av. Vicuña Mackenna 4860, Santiago, Chile

[7] Physics and Astronomy Department, Appalachian State Univ., Boone, NC 28608, USA

[8] Ministerio de Educación de la Provincia de Córdoba, Córdoba, Argentina

[9] Observatorio Astronómico, Universidad Nacional de Córdoba, Córdoba, Argentina

[10] IOTA/ES, Barthold-Knaust-Strasse 8, D-30459 Hannover, Germany

[11] Occultation Section of the Royal Astronomical Society of New Zealand (RASNZ), Wellington, New Zealand

[12] International Occultation Timing Association (IOTA), PO Box 7152, Kent, WA 98042, USA

[13] Samford Valley Observatory, QLD, Australia

[14] ESO, Karl-Schwarzschild-Str. 2, 85748 Garching bei, München, Germany

[15] ESO, Alonso de Cordova 3107, Casilla 19001, Santiago 19, Chile

[16] Software Engineering Department, University of Granada, Spain

[17] Western Sydney Amateur Astronomy Group (WSAAG), Sydney, NSW, Australia

[18] Canberra Astronomical Society, Canberra, ACT, Australia

[19] Observatorio Astronómico Los Molinos, DICYT, MEC, Montevideo, Uruguay

[20] Dpto. Astronomia, Facultat de Ciencias, Uruguay

[21] San Pedro de Atacama Celestial Explorations, Casilla 21, San Pedro de Atacama, Chile

[22] Observatorio El Catalejo, Santa Rosa, La Pampa, Argentina

[23] Observatório do Valongo/UFRJ, Ladeira Pedro Antonio 43, RJ 20.080-090 Rio de Janeiro, Brazil

[24] Observatório Nacional/MCTIC, R. General José Cristino 77, RJ 20921-400 Rio de Janeiro, Brazil

[25] Laboratório Interinstitucional de e-Astronomia - LIneA, Rua Gal. José Cristino 77, Rio de Janeiro- RJ 20921-400, Brazil

[26] Unidad Mixta Internacional Franco-Chilena de Astronomía (CNRS UMI 3386), Departamento de Astronomía, Universidad de Chile, Camino El Observatorio 1515, Las Condes, Santiago, Chile

[27] Federal University of Technology- Paraná (UTFPR/DAFIS), Rua Sete de Setembro, 3165, CEP 80230-901, Curitiba, PR, Brazil

[28] Astronomical Association of Queensland, QLD, Australia

[29] School of Physical Sciences, University of Tasmania, Private Bag 37, Hobart, TAS 7001, Australia

[30] Electrical and Information Engineering Department, University of Sydney, Camperdown, NSW 2006, Australia

[31] Penrith Observatory, Western Sydney University, Sydney, NSW, Australia

[32] Stockport Observatory, Astronomical Society of South Australia, Stockport, SA, Australia

[33] Defence Science & Technology Group, Edinburgh, South Australia

[34] The Heights Observatory, Modbury Heights, South Australia

[35] South African Astronomical Observatory, PO Box 9, Observatory, 7935, South Africa

[36] Department of Earth, Atmospheric, and Planetary Sciences, Massachusetts Institute of Technology Cambridge, MA 02139-4307, United States

[37] National Astronomical Research Institute of Thailand, Siriphanich Building, Chiang Mai 50200 - Thailand

[38]Sociedad Astronómica Granadina, Granada, Spain

[39]Asociación Argentina Amigos de la Astronomía, Av. Patricias Argentinas 550, Buenos Aires, Argentina

[40]Departamento de Ciencias Fisicas, Universidad Andres Bello, Fernandez Concha 700, Santiago, Chile

[41] Ciel & Espace, Paris, France

[42] Makes Observatory,La Réunion, France

[43] Dipartimento di Fisica e Astronomia, Universita di Padova, Italy

[44] Internationale Amateursternwarte e. V., IAS, Hakos/Namibia and Bichlerstr. 46, D-81479 München (Munich), Germany.

[45] Observatorio Astronómico de Albox, Apt. 63, 04800 Albox (Almeria), Spain

[46] INAF - Osservatorio Astrofisico di Arcetri, Largo E. Fermi 5, 50125 Firenze, Italy

[47] Royal Astronomical Society of New Zealand (RASNZ), Wellington, New Zealand

[48] Dunedin Astronomical Society, Dunedin, New Zealand

[49] University of Cape Town, Department of Astronomy, Rondebosch , Cape Town, Western Cape, South Africa, 7700

[50] Department of Physics, University of Namibia, 340 Mandume Ndemufayo Ave, P/Bag 13301, Windhoek, Namibia

[51]IMCCE, Observatoire de Paris, CNRS UMR 8028, Université Lille 1, Observatoire de Lille 1 impasse de l'Observatoire, 59000 Lille, France

[52]Kleinkaroo Observatory, Calitzdorp, St. Helena 1B, P.O. Box 281, 6660 Calitzdorp, Western Cape, South Africa

[53]TMT International Observatory, 100 West Walnut Street, Suite 300, Pasadena, CA 91124, USA

ABSTRACT

Two narrow and dense rings (called C1R and C2R) were discovered around the Centaur object (10199) Chariklo during a stellar occultation observed on June 3, 2013 (Braga-Ribas et al. 2014). Following this discovery, we have planned observations of several occultations by Chariklo's system in order to better characterize the ring and main body physical properties. Here, we use 12 successful Chariklo's occultations observed between 2014 and 2016. They provide ring profiles (physical width, opacity, edge structure) and constraints on their radii and pole position. Our new observations are currently consistent with the circular ring solution and pole position, to within the ± 3.3 km formal uncertainty for the ring radii, derived by Braga-Ribas et al. (2014). The six resolved C1R profiles reveal significant width variations from ~ 5.5 to 7 km. The width of the fainter ring C2R is less constrained, and may vary between 0.1 and 1 km. The inner and outer edges of C1R are consistent with infinitely sharp boundaries, with typical upper limits of one kilometer for the transition zone between the ring and empty space. No constraint on the sharpness of C2R's edges is available. A 1σ upper limit of ~ 20 m is derived for the equivalent width of narrow (physical width < 4 km) rings up to distances of 12,000 km, counted in the ring plane.

Subject headings: Rings - Centaur objects: individual (Chariklo) - Stellar Occultations

1. Introduction

The asteroid-like body (10199) Chariklo is a Centaur object orbiting between Saturn and Uranus. It probably moved recently (~ 10 Myr ago) from the Trans-Neptunian region to its present location, and will leave it on a similar short time scale, due to perturbations by Uranus (Horner et al. 2004). With a radius of 119 ± 5 km, estimated from thermal measurements (Fornasier et al. 2014), it is the largest Centaur known to date, but still remains very modest in size compared to the telluric or giant planets. On June 3, 2013, a ring system was discovered around this small object during a stellar occultation. Two dense and narrow rings, 2013C1R and 2013C2R (C1R and C2R for short) were detected. They are

---

[1]Deceased on 16 July 2017

separated by about 15 km and orbit close to 400 km from Chariklo's center (see Braga-Ribas et al. (2014) for details).

Until 2013, rings were only known around the giant planets. This discovery was thus surprising, and is a key to better understanding of the planetary rings, since they now appear to be more common than previously thought. In particular, the two rings being dense, narrow and (at least for C1R) sharp-edged, they look like several of the dense ringlets seen around Saturn and Uranus (Elliot and Nicholson 1984; French et al. 1991, 2016). In that context, there was a strong incentive for planning more occultation campaigns, first to unambiguously confirm the existence of Chariklo's rings and second, to obtain more information on their physical properties.

While the discovery occultation of June 3, 2013 provided the general ring physical parameters (width, orientation, orbital radius, optical depth,...), several questions are still pending, some of them being addressed in this work: do the rings have inner structures that give clues about collisional processes? How sharp are their edges? What are the general shapes of C1R and C2R? Do they consist of solidly precessing ellipses like some Saturn's or Uranus' ringlets? Do they have more complex proper modes with higher azimuthal wave numbers? Are there other fainter rings around Chariklo? What is the shape of the object itself and its role for the ring dynamics? Based on new results, what can we learn about their origin and evolution, which remains elusive (Sicardy et al. 2016)?

This study is made in a context where material has also been detected around the second largest Centaur, Chiron (again using stellar occultations). The nature of this material is still debated and it could be interpreted as a ring system (Ortiz et al. 2015) or a dust shell associated with Chiron's cometary activity (Ruprecht et al. 2015). Since Chariklo is presently moving close to the galactic plane, stellar occultations by this body are much more frequent than for Chiron, hence a more abundant amount of information concerning its rings. The spatial resolution achieved during occultations reaches the sub-km level, impossible to attain with any of the current classical imaging instruments. This said, the very small angular size subtended by the rings (0.08 arcsec tip to tip, as seen from Earth) have made occultation predictions difficult in the pre-Gaia era.

In spite of those difficulties, we could observe 13 positive stellar occultations (including the discovery one) between 2013 and 2016, from a total of 42 stations distributed worldwide (in Brazil, Argentina, Australia, Chile, La Réunion Island, Namibia, New Zealand, South Africa, Spain, Thailand and Uruguay). Here, we focus on the ring detections (a total of 11 chords recorded after the discovery). We also obtained a total of 12 occultation chords by the main body from 2014 to 2016. Their timings are derived here, but their implications concerning Chariklo's size and shape will be presented elsewhere (Leiva et al., 2017, in

preparation). In Section 2, we present our observations and data analysis. In Section 3 we concentrate on the ring structures (width, inner structures, edge sharpness) and geometry (radius and orbital pole). The ring integral properties (equivalent width and depth) are derived in Section 4, before concluding remarks in Section 5.

2. Observations and Data Analysis

Following the ring discovery of June 3, 2013, we predicted and observed 12 positive stellar occultations by Chariklo and/or its rings between 2014 and 2016. In the following list, we mark in italic the events that led to multi-chord ring detections (thus providing constraints on the ring orientation, as discussed latter). Four occultations were observed in 2014, on February 16 (rings), March 16 (rings), *April 29 (rings and body)* and June 28 (rings and body). In 2015, only two positive detections were recorded on April 26 (rings) and May 12 (body), while six occultations were recorded in 2016: July 25 (body), August 8 (rings and body), August 10 near 14h UT (body), August 10 near 16h UT (body), August 15 (body) and *October 1 (rings and body)*.

2.1. Predictions

Predicting stellar occultations by Chariklo and its rings is a difficult task, as the main body subtends about 25 milliarcsec (mas) as seen from Earth, while the rings have a span of about 80 mas. Thus, to be effective, predictions require accuracies of a few tens of mas on both Chariklo's ephemeris and the star position. To meet this requirement, we used a bootstrapping approach, in which each new detection of occultation is used to improve Chariklo's ephemeris, thus providing a better prediction for the next occultation. This continuous update results in the so-called NIMA ephemeris (Numerical Integration of the Motion of an Asteroid, Desmars et al. 2015) accessible online[2].

The candidate stars for events in 2014 and in 2016 were identified during a systematic search for occultations by TNOs using the *Wide Field Imager* (WFI) at the ESO/MPG 2.2m telescope (Camargo et al. 2014), with typical accuracies of $\sim$ 30 mas. However, for the 2015 season, the candidate stars were observed using only the IAG 0.6m telescope at OPD/LNA in Brazil, with lower accuracy than WFI, resulting in a larger number of missed events (two successes out of six attempts).

---

[2]see http://lesia.obspm.fr/lucky-star/nima/Chariklo/

In the majority of the cases, the occulted star was imaged a few days or weeks prior the event in order to improve the astrometry. If possible the observations were made when Chariklo and the star were in the same Field Of View in order to cancel systematic errors. In those cases, accuracy of the predictions was estimated down to ~ 20 mas.

The last occultation in our list (October 1st, 2016) is special as its prediction was based on the new GAIA DR1 catalog released on September 15, 2016 (Gaia Collaboration et al. 2016). However, the J2000 DR1 star position $\alpha = 18\text{h}16\text{m}20.0796\text{s}$, $\delta = -33°01'10.756''$ (at epoch 2015.0) does not account for proper motion. We estimated the latter by using the UCAC4 star position (under the name UCAC4 285-174081) at epoch 2000 and obtained proper motions in right ascension (not weighted by $\cos(\delta)$) and declination of

$$\mu_\alpha = -0.43 \pm 0.008 \text{ ms/yr}$$
$$\mu_\delta = -2.02 \pm 1.05 \text{ mas/yr.}$$

This provides a star position of $\alpha = 18\text{h}16\text{m}20.0789\text{s}$, $\delta = -33°01'10.760''$ at the epoch of occultation. Combining this result with the NIMA ephemeris (version 9) finally provided a prediction that agreed to within 5 mas perpendicular to the shadow track and 20 seconds in terms of timing, and lead to a multi-chord ring and body detection.

2.2. Observations

The circumstances of the observations (telescope, camera, set up, observers, site coordinates, star information) that lead to ring or main body detections are listed in Table 1. Conversely, the circumstances of negative observations (no event observed) are provided in Table 2. Note that observations were made with both small portable telescopes and larger, fixed instruments. Each detection will be designated herein by the name of the station or by the name of the telescope, if well known.

From the timings of the star disappearance (or "ingress") and re-appearance ("egress") behind Chariklo and/or the rings, the geometry of each occultation was reconstructed, as illustrated in Fig. 1. Currently, Chariklo's size and shape are not known well enough to reconstruct the occultation geometries from the events involving the main body. So, we used instead the ring events (even single-chord) to retrieve those geometries. As a starting point, we assume that the rings are circular with fixed orientation in space, and with the orbital parameters derived by Braga-Ribas et al. (2014), namely a J2000 pole position of $\alpha_p = 10\text{h}05\text{m}11.0016\text{s}$, $\delta_p = +41°28'32.4891''$ and respective radii $a_{C1R} = 390.6$ km and $a_{C2R} = 404.8$ km for the two rings. The reconstructed geometry allows us to derive the observed position of Chariklo center (reported in Table 1). If the star position was perfect,

this derived position must coincide with the occulted star position. The difference between the two positions is the offset between the predicted and the observed Chariklo's position. This offset is implemented in NIMA after each occultation, in order to improve Chariklo's ephemeris.

If the rings are *not* circular, this will impact their pole position and will eventually be visible as discrepancies between observations and predictions. The pole position problem is discussed further in Section 3.4.

Note that some stations did not detect any ring occultations, whereas they should have considering the occultation geometry, see Reedy Creek on May 12, 2015 and Sydney on August 10, 2016. Data analysis shows that those non-detections are actually consistent with the low signal-to-noise-ratio (SNR) obtained at those stations. Thus, secondary events have always been detected if SNR was high enough. This leads us to conclude that C1R (which always dominates the profile) is continuous. Same conclusion on C2R is more ambiguous as C2R was usually blended together with C1R. Nevertheless, we will assume that C2R is continuous in this paper.

2.3.   Data Reduction

After a classical data processing that included dark subtraction and flat fielding, aperture photometry provided the stellar flux as a function of time (the date of each data point corresponding to mid-exposure time), the aperture being chosen to maximize SNR. The background flux was estimated near the target and nearby reference stars, and then subtracted, so that the zero flux corresponds to the sky level. The total flux from the unocculted star and Chariklo was normalized to unity after fitting the light curve by a third or forth-degree polynomial before and after the event. In all cases, a reference star (brighter than the target) was used to correct for low frequency variations of the sky transparency.

The light curves are displayed in Fig. 3 and 4, each of them providing a one-dimensional scan across Chariklo's system, as projected in the sky plane. In some cases, the readout time between two frames caused a net loss of information as photon acquisition was interrupted during those "dead time" intervals. The flux statistics provides the standard deviation of the signal, which defines the 1σ error bar on each data point which was used latter for fitting diffraction models to ingress and egress events. Note that during an occultation by the main body, the stellar flux drops to zero, but the flux in the light curve is not zero, as it contains Chariklo's contribution, and in one case, the flux from a nearby companion star, see below.

2.4. The case of the double star of April 29, 2014

This event, observed from South Africa (see Table 1), revealed that the occulted star was a binary. As seen from Springbok, the primary star ("A") was occulted by C1R and C2R (but missed the main body), while the fainter companion star ("B") disappeared behind Chariklo along an essentially diametric chord at Springbok (Fig. 1). Because the component B was about 9 times fainter than A (see below), and considering the drop of A caused by C1R at Springbok, we expect a short drop in the light curve of only 8% due to the disappearance of component B behind C1R. This is too small to be detected, in view of the SNR of about 7 per data point obtained at that station (Fig. 4).

Meanwhile in Gifberg, we obtained only a grazing occultation of the primary star by C2R (Fig. 1). This provides the best profile of that ring ever recorded (see Section 3.3). Finally, at the South African Astronomical Observatory (SAAO), only the component B was occulted by the rings, while the main star missed both the rings and the main body (Fig. 1). However, due to the high SNR obtained at that station, the partial drop caused by the rings on component B has about the same useful SNR as the drop of component A as seen from the smaller telescope at Springbok.

For the Springbok light curve, we can estimate the flux ratio Φ_A/Φ_B between the two stars by considering the drop of component B caused by Chariklo. In doing so, we can neglect Chariklo's contribution to the total flux. From Chariklo's absolute magnitude, $H_V = 7.0$ in 2014 (Duffard et al. 2014), and heliocentric and geocentric distances of 14.8 au and 14.1 au during the event, respectively, we obtain a Chariklo apparent magnitude ~ 18.6. This is 5.6 magnitudes fainter than the star, which has V=13.0 (NOMAD catalog[3]), meaning that Chariklo contributed to the total flux of less than 0.6%, a negligible value at our level of accuracy.

The fractional drop observed during the occultation of B by Chariklo provides its partial contribution to the total stellar flux, $\Phi_B = 0.1036 \pm 0.0075$ (Fig. 5). This implies a flux ratio $(\Phi_A/\Phi_B)_{TC247} = 8.65 \pm 0.65$, as measured by the Texas Instruments TC247 array used at Springbok (in broad band mode, no filter). This directly provides the baseline level for the occultations of A by the rings (Figs. 5 and 8), i.e. the level that corresponds to a total disappearance of component A.

A similar calibration is not possible for the SAAO ring events, as that station did not record an occultation by the main body. Moreover, the ratio $(\Phi_A/\Phi_B)_{TC247}$ cannot be used, as the SHOC instrument (see Coppejans et al. 2013) used at SAAO (also in broad band

---

[3]See http://vizier.u-strasbg.fr/viz-bin/VizieR

mode) has a different spectral response, so that the ratio depends on the color of the two stars.

To proceed forward, we have used the B, V, K magnitudes of the star (taken from the Vizier page, in NOMAD catalog). We have generated combined synthetic spectra energy distribution of the two components, and using various (and separate) effective temperature T_{eff} for A and B. The effect of interstellar reddening has been parametrized using the color excess $E(B-V)$. We adopted the classical total to selective extinction parameter $R_V = 3.1$ for Milky Way dust from Fitzpatrick (1999). The relative contributions of each component were adjusted in order to fit both the observed magnitude of the star and the flux ratio as observed with the TC247 array. Finally, accounting for the spectral response of the Andor array, we can then estimate the ratio $(\Phi_A/\Phi_B)_{\mathrm{Andor}}$ for that detector.

A difficulty stems from the fact that there is a degeneracy between the effective temperatures assumed for the two components, $T_{\mathrm{eff}}(A)$ and $T_{\mathrm{eff}}(B)$. The star B cannot be much cooler than A, otherwise its diameter would be larger and strong signatures in the near IR would appear in the composite spectrum. We have opted for a difference $T_{\mathrm{eff}}(A) - T_{\mathrm{eff}}(B) \sim 1000$ K, and assume that the two stars are on the main sequence. We find a good fit to the observed magnitudes with $T_{\mathrm{eff}}(A) = 5000$ K and $T_{\mathrm{eff}}(B) = 4000$ K, and then a ratio $(\Phi_A/\Phi_B)_{\mathrm{Andor}} = 7.66$, corresponding to a contribution to the total flux of $\Phi_A = 0.885 \pm 0.025$ for component A, where the error bar is estimated from the typical possible ranges for $T_{\mathrm{eff}}(A)$ and T_{eff}.

Finally, we can estimate the apparent diameter of each component projected at Chariklo's distance: $\theta_A = 0.199 \pm 0.015$ km and $\theta_B = 0.092 \pm 0.015$ km. Those values will be used latter when fitting the ring profiles with models of diffracting, semi-transparent bands.

Assuming the ring radii and pole orientation of Braga-Ribas et al. (2014), see also Section 2.2, and using the ring detections in Springbok, Gifberg and SAAO, we deduce that star B was at angular distance 20.6 mas from star A as projected in the sky plane, with position angle $P = 209.8°$ relative to the latter (where P is counted positively from celestial North towards celestial East).

3. Ring events analysis

3.1. Profiles fitting

In order to determine accurate and consistent timings of the ring occultations, we use a "square-well model" in which each ring is modeled as a sharp-edged, semi-transparent

band of apparent opacity p' (along the line of sight) and apparent width (in the sky plane) $W_\perp$. We use the numerical schemes described in Roques et al. (1987) to account for Fresnel diffraction, stellar diameter projected at Chariklo's distance, finite bandwidth of the CCD, and finite integration time of the instrument. Finally, considering projection effects, we can derive the ring physical parameters (radial width, normal opacity, etc...) and orbital elements, see Appendix for details.

For sake of illustration, we give various parameters of interest in the case of the April 29, 2014 occultation. The Fresnel scale $F = \sqrt{\lambda D/2}$ for Chariklo's geocentric distance at epoch, $D = 2.11 \times 10^9$ km is 0.83 km, for a typical wavelength of $\lambda = 0.65\,\mu$m. The projected stellar diameters have been estimated above to 0.199 ± 0.015 km and 0.092 ± 0.015 km for the primary star and secondary star, respectively (see Section 2.4). The smallest cycle time used during that campaign was 0.04 s (at SAAO), corresponding to 0.5 km traveled by the star relative to Chariklo in the celestial plane. Consequently, the light curves are dominated by Fresnel diffraction, but the effects of stellar diameters and finite integration time remain comparable. Similar calculations for the other twelve occultations show that the effect of finite integration time dominated in all those cases.

The synthetic ring profiles are then fitted to observations so as to minimize the classical χ^2 function:

$$\chi^2 = \sum_i \frac{(\Phi_{i,\mathrm{obs}} - \Phi_{i,\mathrm{calc}})^2}{\sigma_i^2} \tag{1}$$

where Φ is the flux, i refers to the ith data point, "obs" refers to observed, "calc" refers to calculated, and σ the 1σ-level error of the ith data point. The free parameters of the model are described in the next subsection. The 1σ error bar on each parameter is estimated by varying this particular parameter to increase χ^2 from the best value χ^2_{min} to $\chi^2_{min} + 1$, the others parameters are set free during this exploration.

3.2. Mid-times and widths of the rings

The best fitting square-well model described above provides relevant parameters that depend on the occulting object. Three cases are possible: occultations by (1) main body; (2) resolved rings; (3) unresolved rings. The relevant parameters in each case are respectively (1) the times of ingress and the egress of the star behind the body; (2) the mid-time of the occultation t_0, the radial width *reprojected in the plane of the rings*, W_r, and the local normal opacity p_N for each ring (see Appendix for details); (3) the mid-time of the occultation. Those parameters are listed in Table 4 (resolved ring events), Table 5 (unresolved ring events), and in Table 6 (main body events). The best fits for each occultation are plotted in Fig. 3 and

4 (ring occultations) and in Fig. 5 (main body occultations).

The grazing occultation by C2R recorded in Gifberg (Fig. 1) requires a special analysis. In this geometry, the radial velocity of the star relative to the ring changes significantly during the event (while it is assumed to be constant for all the other events). To account for this peculiarity, we first converted the light curve (time, flux) into a profile (Δr, flux), where Δr is the radial distance to the point of closest approach to Chariklo's center (in the sky plane). Then we can apply the square-well model as explained in section 3.1, except that the flux is now given in terms of Δr, instead of time. Best fits for ingress and egress are plotted in Fig. 6.

Table 4 summarizes the values of W_r for each resolved profile. Fig. 7 shows W_r vs. the true longitude L counting from the ascending node. Accounting for the most constraining events, W_r varies between 5 km and 7.5 km in C1R and between 0.05 km and 1 km in C2R (at 1σ-level). Fig 7 could constrain the rings proper mode. Unfortunately, the true longitude L plotted in Fig. 7 (and latter in Fig. 11) is not the correct quantity to use in order to detect $m = 1$ proper modes (the true anomaly $L - \varpi$ should be used instead of L, where ϖ is the longitude of periapse). As the precession rates of the rings are unknown, no conclusion can be made. Nevertheless, those width variations are observed both for a given occultation at different longitudes and for different occultations at different dates, see Fig. 7. Implications are discussed in Section 6.

3.3. Ring inner structures

Fig. 8 shows the best radial profiles of the rings that we have obtained so far, taken from the discovery observation of June 3, 2013 and the April 29, 2014 event. They are currently the only profiles that clearly resolve C1R from C2R, and in the case of the April 29, 2014 event, the only profiles that resolve C1R. A W-shape structure inside C1R is clearly seen at egress in the Springbok and SAAO profiles, and marginally detected in the Springbok ingress profile, while being absent (to within the noise) in the SAAO ingress profile.

Note that small (2-4 km) variations of radial distances between the two rings are visible in Fig. 8. The average gap distance between the two rings on the six profiles is thus 14.8 km.

Since the origin of radial distance has been fixed *arbitrarily* on the center of C2R, it is not possible to attribute those variations to an eccentricity of C1R, C2R or both. Note also that the April 29 profiles are montages obtained by juxtaposing the profiles of C1R recorded at Springbok and SAAO and the profile of C2R recorded in Gifberg. So, they scan different rings longitudes, and conclusions based on this plot can only be qualitative.

3.4. Ring pole

By analogy with their Uranian counterparts, we expect that Chariklo's ring orbits have essentially elliptical shapes, corresponding to a normal mode with a $m = 1$ azimuthal harmonic number. Moreover, other modes with higher values of m are possible and the two rings may not be coplanar. However, data on Chariklo's rings are currently too scarce to reach those levels of details. Instead, we have to simplify our approach, considering the observational constraints at hand.

The simplest hypothesis is to assume that the two are circular, concentric and coplanar. Then, their projections in the sky plane are ellipses characterized by $M = 5$ adjustable parameters: the apparent semi-major axis a', the coordinates of the ellipse's center (f_c, g_c), the apparent oblateness $\epsilon' = (a' - b')/a'$ (where b' is the apparent semi-minor axis), and the position angle P of the semi-minor axis b'. For circular rings, $\epsilon' = 1 - \sin(B)$, where B is the ring opening angle ($B = 0$ and $B = 90°$ corresponding to edge-on and pole-on geometries, respectively).

Note that (f_c, g_c) is related to the offsets in right ascension and declination between the predicted and observed positions of the object, relative to the occulted star. The positions of Chariklo deduced from (f_c, g_c) – at prescribed times and for given star positions – are listed in Table 1. They can be used to improve Chariklo's ephemeris, once the star positions are improved, using the DR1 Gaia catalog and its future updates.

This circular ring model requires at least $N \geq M = 5$ data points in order to provide a unique solution for the ring radius a (coincident with a') and its J2000 pole position (α_p, δ_p). Only the June 3, 2013 discovery observation with 7 chords (and thus $N = 14$ data points corresponding to the chord extremities) has sufficient constraints to provide unambiguous ring orbits. More precisely, as only one instrument (Danish telescope) could resolve the rings C1R and C2R in 2013, this multi-chord event mainly determines the orbit of C1R, which largely dominates the usually blended ring profiles. Then we assumed that C2R is coplanar with C1R and separated radially from it by a constant distance $\Delta a = 14.2 \pm 0.2$ km (Braga-Ribas et al. 2014).

The April 29, 2014 event provides two chords ($N = 4$ data points) on C2R. This allows us to definitely eliminate one of the pole positions derived from the 2013 event. Actually, determining the angles B and P at a given date provides *two* possible pole positions, 1 and 2, depending on which part of the rings, as seen in the sky plane, is the "near arm" or the "far arm", see Braga-Ribas et al. (2014) for details. The C2R chord observed at Springbok turned out to be longer than the longest possible length allowed by solution 2, thus confirming that the preferred solution 1 of Braga-Ribas et al. (2014), based on the long-term photometric

behavior of Chariklo (see also below), was actually the correct one.

In order to constrain the pole position, even with $N < M$, we vary the couple (P, B) in a predetermined grid, while the other three parameters are adjusted in order to minimize the radial residuals in the sky plane relative to the ring center. Since the pole position is given by two parameters (α_P, δ_P), the 68.7% confidence domain (called 1σ-level here) is obtained by allowing variations of the χ^2 function from $\chi^2_{\min}$ to $\chi^2_{\min} + 2.3$ (Press et al. 1992), and by selecting values of a to ± 3.3 km, the nominal error on the C1R and C2R radii: $a_{C1R} \sim 391$ km and $a_{C2R} \sim 405$ km (Braga-Ribas et al. 2014) . The pole position derived from the April 29, 2014 occultation is displayed in Fig. 9. Note that it is consistent with but less accurate than the pole determined in 2013.

Finally, the October 1st, 2016 event also provided two chords ($N = 4$ data points) across the rings, but without resolving C1R from C2R (Fig. 4). Thus, we assumed that the profiles are dominated by C1R, and derived the pole position displayed in Fig. 9. It is again consistent with the poles of 2013 and 2014, but with larger error bars due to the ill-configured chord geometry (nearly diametric) that permits more freedom on the pole position (Fig. 1).

Further constraints are in principle provided by the long-term photometric behavior of Chariklo's system between 1997 and 2014, as compiled by Duffard et al. (2014), see their Fig. 1. The observed photometric variations can be explained by the changing viewing geometry of the rings, linked itself to the pole orientation. Contrary to the occultation data, the photometric variations do not depend on the particular shape of the rings (e.g. circular vs. elliptic). Fitting for the pole position and accounting for the error bars taken from Duffard et al. (2014), we obtain the possible domain shown in Fig. 9. Note that it is consistent with but less accurate than all our occultation results.

From Fig. 9 we can conclude that our current data set (spanning the 3-year interval 2013-2016) is consistent with circular rings that maintain a fixed pole in space, and to within the current formal error bar on the semi-major axis a (± 3.3 km). Note that the extensions of the error domains for the pole position (colored regions in Fig. 9) are dominated by the errors in the data (i.e. the timings of the ring occultations), not by the formal error for a quoted above. In other words, even if the ring shape were known perfectly, the pole position would not be significantly improved compared to the results shown in Fig. 9. A Bayesian approach could be used to estimate the probability that the rings are elliptic, considering the data at hand and assuming a random orientation for the ring apsidal lines. Considering the paucity of data and the large number of degrees of freedom, this task remains out of the scope of the present paper. In any case, new observations will greatly help into this approach by adding more constraints on the ring shapes and orientations.

For all the other ring single-chord detections ($N = 2$ data points), neither the rings radii nor their pole position can be constrained. Instead, assuming the pole orientation of Braga-Ribas et al. (2014), we determined the ring center, also assumed to coincide with Chariklo's center of mass. Having only one ring chord introduces an ambiguity as two solutions (North or East of the body center) are possible. However, in all cases but one (August 8, 2016) it was possible to resolve this ambiguity as the absence of detections made by other stations eliminated one of the two solutions. For the August 8, 2016 event, the ambiguity remains, and we give the two possible Chariklo's positions, see Table 1.

None of the single chords are longer than the longest chord expected from the Braga-Ribas et al. 2014's solution, and thus remain fully consistent with that solution.

3.5. Sharpness of C1R edges

A striking feature of the resolved C1R profiles from the April 29, 2014 event is the sharpness of both its inner and outer edges. This is reminiscent of the Uranian rings (Elliot et al. 1984; French et al. 1991), and might stem from confining mechanisms caused by nearby, km-sized shepherding moonlets (Braga-Ribas et al. 2014). In order to assess the sharpness of C1R's edges, we use a simple model, where each edge has a stepwise profile, as illustrated in Fig. 10. Instead of having an abrupt profile that goes from apparent opacity 0 to p', we add an intermediate step of radial width in the ring plane Δw_r and opacity $p'/2$ around the nominal ingress or egress times, as deduced from the square-well model described before, see also Table 4. With that definition, Δw_r is a measure of the typical edge width, i.e. the radial distance it takes to go from no ring material to a significant optical depth.

We explored values of Δw_r by varying the χ^2 function (Eq. 1) from its minimum value $\chi^2_{\min}$ to $\chi^2_{\min} + 1$. The results are listed in Table 3 and illustrated in Fig. 10. Note that all edges are consistent with infinitely sharp edges ($\Delta w_r = 0$) to within the 1σ level and that upper limits for Δw_r are typically 1 km. No significant differences are noticeable between the inner and the outer edges, contrary to, e.g., some Uranian rings (French et al. 1991).

Note finally that the width of C2R, as derived from the grazing event in Gifberg (Fig. 6) is slightly smaller (~ 0.7 km) than the Fresnel scale (~ 0.8 km). As such, it is not possible to assess the sharpness of its edges.

4.   Integral properties of rings: equivalent width and depth

We now turn to the measure of the ring's equivalent width E_p and equivalent depth A_τ, two quantities defined and discussed by Elliot et al. (1984) and French et al. (1991), as detailed in the Appendix. Those quantities are physically relevant, as they are related to the amount of material present in a radial cut of the ring, in the extreme cases of monolayer and polylayer rings, respectively.

The values of E_p are given in Table 4 (resolved events) and in Table 5 (unresolved events). For the resolved profiles, we have plotted E_p against the radial width W_r in Fig. 11. Implications in terms of mono- versus polylayer models will be discussed in Section 6. For the profiles that resolve C1R from C2R (and where both rings were detected), and those where the two profiles are blended (the majority of our observations), we have plotted the *integrated* $E_p(1+2)$ against the true longitude L (counted from the J2000 ring plane ascending node) in Fig. 11. From that figure, we see that the values of $E_p(1+2)$ lie in the interval 1-3 km, with no significant differences between the various measurements. In other words, no significant variations of $E_p(1+2)$ with time and/or longitude are detected in our data set.

In this *preliminary* study, the rings are considered as one entity C1R + C2R but further studies should treat them independently to derive conclusions on the structure of each of them.

5.   Search for faint ring material

The best light curve available in terms of photometric quality is from the Danish Telescope. It was acquired at a rate of 10 frames per second during the 30 minutes bracketing the occultation of June 3, 2013 (Braga-Ribas et al. 2014). It can be used to search for additional material orbiting Chariklo, assuming semi-transparent, uninterrupted, and permanent rings coplanar to C1R and C2R.

For this purpose, we consider the equivalent width $E_p(i)$ of the putative ring material intercepted during the acquisition interval $\Delta t(i)$ corresponding to the ith data point, and counted radially in the ring plane. Using the results of the Appendix (see also Boissel et al. 2014 for details), we obtain

$$E_p(i) = \frac{|\sin(B)|}{2}[1 - \phi(i)]\Delta r(i) \tag{2}$$

where $\Delta r(i)$ is the radial interval travelled by the star during $\Delta t(i)$ (projected in the ring plane), and where $\phi(i)$ is the normalized stellar flux. Due to projection effects, the value of

$\Delta r(i)$ varied between the extreme values of 3 to 4 km during the acquisition interval, which sets the radial resolution of this particular data set.

The values of $E_p(i)$ vs. radial distance r is displayed in Fig. 12. Note that the light curve probes radial distances of up to $\sim 12,000$ km, about 30 times the ring radii. Using bins of width 60 km, we evaluate the variance of the *difference* between two consecutive points in each box, thus eliminating low frequency variations of $E_p(i)$. Dividing this variance by two (to account for the fact that the data points are uncorrelated) and taking the square root, we obtain the 1σ level, standard deviation of $E_p(i)$, denoted $E_p(1\sigma)$, see the red line in Fig. 12. The value of $E_p(1\sigma)$ remains stable in the entire range considered here, with typical values of 20 m. Thus, at the 1σ level, we do not detect narrow ($W_r < $ 3-4 km) rings coplanar with C1R and C2R with equivalent width larger than about 20 meters. This is about ten times fainter than the equivalent width of C2R (Fig. 11). Note that this limit corresponds to extreme cases of either opaque rings with width ~ 20 m, or semi-transparent rings of width $\sim$ 3-4 km and normal opacity 0.007-0.005, and all the intermediate solutions that keep $E_p(i)$ at 20 m.

6. Concluding remarks

We detected Chariklo and/or its rings during a total of thirteen stellar occultations between 2013 and 2016. They demonstrate beyond any doubt that this Centaur is surrounded by a system of two flat rings, C1R and C2R. All the observations at hand are consistent with the circular ring solution of Braga-Ribas et al. (2014), with C1R orbiting at 391 ± 3 km from Chariklo center and with C2R orbiting outside C1R at an average distance of 14.8 km (Fig. 8). This definitely rules out interpretations of the initial observation of June 3, 2013 by a 3D dust shell, or a set of cometary-type jets being ejected from the surface of the body. In fact, the changing aspect of the rings seen during the occultations is entirely attributable the changing position of Chariklo relative to Earth, with a ring pole position that remains fixed in space (Fig. 9).

Our best resolved observation (April 29, 2014) reveals a W-shaped structure inside the main ring C1R (Fig. 8). Moreover, the radial width W_r of C1R measured on the best profiles exhibits significant variations with longitude, with a peak to peak variation of $\delta W_r \sim 2.5$ km between 5 and 7.5 km, see Table 4 and Fig. 7. All the resolved profiles of C1R exhibit edges that are consistent with infinitely sharp boundaries, once diffraction and star diameter effects are accounted for. The typical 1σ upper limits for the edge transition zones is about one kilometer (Table 3 and Fig. 10). Note finally that none of our observations permits to resolve the profile of ring C2R, whose width is constrained between 100 m to 1 km (Fig. 11).

Remarkably, C1R properties (W-shaped profile, variation of width with longitude and sharp edges) are reminiscent of the narrow eccentric ringlets found around Saturn (French et al. 2016) or Uranus (Elliot and Nicholson 1984; French et al. 1991). The maintenance of apse alignment could be due to self-gravity (Goldreich and Tremaine 1979), viscous effects at the edges (Chiang and Goldreich 2000), or a combination of self-gravity and viscous effects (Mosqueira and Estrada 2002). If validated, those models may provide insights into the ring physical parameters. For instance, the overdensities of material at some 100's m from the edges (as seen in Fig. 8) is predicted by viscous models and deserve more detailed observational support in the case of Chariklo. Also, the measure of the eccentricity gradient across the rings, q_e, could be related to the surface density of the ring material, once Chariklo's dynamical oblateness J_2 is known (Pan and Wu 2016). However, our current data set is too fragmentary for drawing any reliable conclusions in that respect, since both a comprehensive ring orbit model and the knowledge of Chariklo's J_2 are missing.

In their simplest forms, the Saturn or Uranus ringlets are described as sets of nested elliptical streamlines, with a width that varies as $W_r = [1 - q_e \cos(f)]\delta a$, where f is the true anomaly, $q_e = a\delta e/\delta a$ measures the eccentricity gradient across the ring, δa and δe being the changes of the semi-major axis a and eccentricity e across that ring. Consequently, the interpretation of Fig. 7 remains ambiguous, since only the true longitude corresponding to the events is currently known, while the true anomaly f is unknown. In fact, any (expected) apse precession between observations impairs a correct interpretation of that figure. At this point, only the total eccentricity variation across the ring can be estimated, i.e. $\delta e = \delta W_r/2a \sim 0.003$ from the estimations of W_r and a given above. This sets a lower limit of the same order for e, close to the eccentricity of Uranus' ϵ ring, 0.008 (French et al. 1991).

A much better case for modeling the rings would be to derive W_r vs. the ring radial excursion $r - a$ relative to the mean radius r. The formula above predicts a linear behavior, u. Unfortunately, the ring center is currently undetermined: we assume on the contrary a circular ring to derive it, and determine its pole. The fact that the circular hypothesis provides satisfactory fits to our data, to within the accuracy of C1R's radius determination (some ± 3 km), suggests that $r - a$ should also vary by a few kilometers at most. In any case, the degeneracy between the ring eccentricity and its pole position can be lifted by obtaining several multi-chord occultations and more accurate pole positions than shown in Fig. 9 (and thus distinguish between projection and eccentricity effects). Also, as expected apsidal precession rates are of the order of a couple of months (Sicardy et al. 2016), observations closer than that in time should be done to derive Chariklo's J_2.

Turning now to the integral properties of the rings, we have determined the equivalent

widths E_p of C1R and C2R, when resolved, and the sum of the two when unresolved (Fig. 11). We see that C1R, with $E_p(C1R) \sim 2$ km, contains about ten times more material than C2R, $E_p(C2R) \sim 0.2$ km. On one hand, if the equivalent width is constant within radial width, the ring can be considered as monolayer (French et al. 1986), as no shadowing by neighboring particules occurs (except in nearly edge-on view). On the other hand, if the ring is polylayer, the equivalent depth is independent from W_r. In that latter case, the equivalent width can be expressed as a function of ring width W_r and the constant value of equivalent depth $\bar{A}_\tau$:

$$E_p(W_r) = W_r(1 - \mathrm{e}^{-2\bar{A}_\tau/W_r}) \tag{3}$$

(this equation, based on the work of French et al. 1986 has been corrected by the factor 2 in optical depth due to the diffraction by ring particles - see Appendix). Fig. 11 shows E_p vs. W_r assuming several values of $\bar{A}_\tau$ between 1.15 and 2 km for C1R and between 0.15 and 0.4 km for C2R (no real measurement of this parameter has been made in this work, the lines show the expected trends - see Appendix). Contrary to French et al. (1986), the data do not allow any discrimination between E_p or A_τ constant within the radial width. Thus, no choice between the mono- or polylayer models can be made.

Finally, we have searched for faint material ring around the already discovered rings. The best data set at hand provides 1σ upper limits of ~ 20 m for the equivalent width of narrow ($< 3\text{-}4$ km physical width) rings coplanar with C1R and C2R, up to distances of $12,000$ km (counted in the ring plane). Note that in 2015, direct images of Chariklo have been recorded using HST and SPHERE (Sicardy et al. 2015a,b). The goal was to image the rings and/or look for possible shepherd satellite(s) and jets. Considering material of same albedo as the rings (p=0.1), following limits have been inferred: (1) no satellite bigger than ~ 2 km (being brighter than $V \sim 26.1$) up to 6400 km (~ 8 times the ring size) from Chariklo center. (2) no satellite bigger than ~ 1 km ($V \sim 27.5$) up to 8 arcsec. For comparison the Hill radius is 7.5 arcsec. (3) no jet, coma or material brighter than $V \sim 28$ corresponding to jets of width ~ 10 km or material of optical depth of around 2×10^{-5} per pixel. Note that HST resolution did not allow to look closer than 1000 km from Chariklo's center, so the rings were not detected.

Future observations will benefit greatly from the Gaia catalog. A flavor of it has been provided by the Gaia-based prediction of the October 1$^\text{st}$, 2016 occultation, which turned out to be correct to within 5 mas in declination (respectively 9 mas in right ascension), corresponding to about 50 km (respectively 90 km). The improvement of Chariklo's orbit stemming from successful occultation observations and the sub-mas accuracy of forthcoming Gaia catalogs will provide predictions accurate to the few-kilometer level. This will allow a much better distribution of stations (using portable instruments), with an optimal ring longitude coverage aimed at improving the ring orbital models. It will also be possible to

plan multi-wavelength observations to constrain the ring particle sizes. Multi-wavelength instruments are rare, and difficult to obtain unless a strong case is made, based on reliable predictions. Higher SNR light curves will also be obtained in order to calculate the equivalent depths of both rings and definitely answer if the rings are monolayer or polylayer. Finally, the Gaia catalog will allow a much better coverage of Chariklo's limb, which is currently poorly mapped. The general shape and local irregularities of the body will in turn have important consequences for a better understanding of the ring dynamics.

A. Appendix: Equivalent width and equivalent depth definitions

We define p' as the *apparent* opacity of the ring. It measures the fractional drop of stellar flux $1 - I/I_0$ as observed from Earth (where I_0 and I are the incident and transmitted fluxes, respectively). Thus, $p' = 0$ means a transparent ring and $p' = 1$ means an opaque ring. By "apparent", we mean here as observed from Earth in the plane of the sky. The apparent quantities will be primed hereafter to distinguish them for the actual quantities at the level of the ring, see below. The apparent ring optical depth is defined as $\tau' = -\ln(1 - p')$.

Appropriate transformations, accounting for the ring opening angle B and distance D to the ring, must be applied to derive the opacity p_N and optical depth τ_N at the ring level, where "N" means normal to the ring plane. Once this is done, one may define the equivalent width E_p and equivalent depth A_τ of the ring as the integrals of p_N and τ_N, respectively, over the ring radial profile of width W_r (measured radially in the plane of the ring):

$$E_p = \int_{W_r} (v_r p_N) dt \tag{A1}$$

$$A_\tau = \int_{W_r} (v_r \tau_N) dt, \tag{A2}$$

where v_r is the radial velocity of the star relative to Chariklo in the ring plane.

The quantities E_p and A_τ are relevant for two extreme cases of ring structures. One is a monolayer ring, in which case $p_N = |\sin(B)| \cdot p$ (for $|\sin(B)| \leq 1/p$), where p is the ring opacity as seen under an opening angle B. The other model is a polylayer ring (where the ring thickness is much larger than the particle sizes), in which case $\tau_N = |\sin(B)| \cdot \tau$, where τ is the ring optical depth, seen again under an angle B, see details in Elliot et al. (1984).

In principle, E_p and and A_τ can be determined by numerically performing the integrations $|\sin(B)| \cdot \int (v_r p) dt$ and $|\sin(B)| \cdot \int (v_r \tau) dt$ over the observed profiles. Since the convolutions of the profiles by both Fresnel diffraction and stellar diameter conserve energy, those integrations provide the correct values of E_p and and A_τ. Those two quantities are

eventually measures of the amount of material (per unit length) contained along a radial cut of the ring, in their respective domains of validity (monolayer vs. polylayer), see French et al. (1991).

However, complications arise because of two effects: (1) the ring is not an uniform screen of opacity p, but rather a set of many particles that cover a fractional surface area p of the ring, while individually diffracting the incoming wavefront, and (2) in several cases, the ring profiles are not resolved, i.e. the entire stellar drop occurs inside an individual acquisition interval, thus "diluting" the opacity p over that interval. We now comment these points in turn.

First, individual ring particles of radius r diffract the incoming wave (with wavelength λ) over an Airy scale $F_A \sim (\lambda/2r)D$, as seen by the observer at distance D from the rings. With $r \sim$ of a few meters and $D \sim 2\times10^9$ km, and using wavelengths in the visible range, we obtain $F_A >\sim 500$ km, which is significantly larger than typical values of a few kilometers for $W_\perp$, the width of ring as seen in the sky plane. This results in a loss of light in the occultation profiles, making the rings appear more opaque than they actually are. It can be shown that the ring apparent optical depth τ' (in the sky plane) is actually twice as large as its actual value τ, i.e. the one would have for an observer close to the ring: $\tau' = 2\tau$, see Cuzzi (1985). An equivalent way to describe that effect is to note that the actual ring opacity p is related to p' by $(1 - p)^2 = 1 - p'$. Thus, the ring acts as a screen of amplitude for the incoming wave, instead of screen of intensity, see details in Roques et al. (1987).

If the ring profile is resolved, it is enough to estimate numerically the integrals:

$$E_p = |\sin(B)| \cdot v_r \int_{\text{profile}} (1 - \sqrt{1 - p'})dt \tag{A3}$$

$$A_\tau = -\frac{|\sin(B)|}{2} \cdot v_r \int_{\text{profile}} \ln(1 - p')dt \tag{A4}$$

The second point to examine is the fact that the ring profile may not be resolved during the integration time Δt. In this case p' is not known, and the integrals above cannot be evaluated without an independent piece of information. Let us consider the simple case of a uniform opacity p across the ring profile (square-well model). Then, the apparent equivalent width $E' = p'W_\perp$ (where $W_\perp$ is the width of the ring as observed in the sky plane) can be evaluated from energy conservation by $E' = f'v_\perp\Delta t$, where $v_\perp$ is the velocity of the star normal to the ring in the sky plane, and f' is the fractional stellar drop during Δt. From the definition of E_p above (Eq. A3) and from $(1 - p)^2 = 1 - p'$, one obtains:

$$E_p = |\sin(B)|\frac{v_r}{v_\perp} \cdot \frac{E'}{2 - p} \tag{A5}$$

Since $0 \leq p \leq 1$, we have:

$$|\sin(B)| \cdot \frac{v_r}{v_\perp} \cdot \frac{E'}{2} \leq E_p \leq |\sin(B)| \cdot \frac{v_r}{v_\perp} \cdot E', \tag{A6}$$

i.e. a uncertainty factor of two, depending on the assumption on p.

For unresolved events, the fit of the best square-well model to the data allows measurements of E_p. The problem is that p is badly constrained ($0 \leq p \leq 1$) by the fits. Eq. A6 shows that error bars will be much larger than for resolved events. It could be possible to solve that problem by noting that $p' = E'/W_\perp = (E'/W_r)(v_r/v_\perp)$. As we know W_r we can constrain p', and thus E_p. Assuming that $W_{r,C1R+C2R}$ lies between 3 and 14 km (see Table 4), the error bars values of E_p remain similar to those without the width constraint. As we are not certain that 3 and 14 km are the width minimum and maximum, we choose not to use this constraint.

Note that the case of A_τ is in general harder to solve. Even when the profile is resolved, the densest parts of the ring have high opacities $p' \sim 1$, and thus large uncertainties on $\tau' = -\ln(1-p')$ stemming from the data noise and uncertainties on the baseline levels (Fig. 8). Consequently, we have not attempted to derive A_τ for our current data set.

REFERENCES

Boissel, Y., Sicardy, B., Roques, F., Gaulme, P., Doressoundiram, A., Widemann, T., Ivanov, V.D., Marco, O., Mason, E., Ageorges, N., Mousis, O., Rousselot, P., Dhillon, V.S., Littlefair, S.P., Marsh, T.R., Assafin, M., Braga Ribas, F., da Silva Neto, D., Camargo, J.I.B., Andrei, A., Vieira Martins, R., Behrend, R., Kretlow, M., 2014. An exploration of Pluto's environment through stellar occultations. Astron. Astrophys. 561, A144.

Braga-Ribas, F., Sicardy, B., Ortiz, J.L., Snodgrass, C., Roques, F., Vieira-Martins, R., Camargo, J.I.B., Assafin, M., Duffard, R., Jehin, E., Pollock, J., Leiva, R., Emilio, M., Machado, D.I., Colazo, C., Lellouch, E., Skottfelt, J., Gillon, M., Ligier, N., Maquet, L., Benedetti-Rossi, G., Gomes, A.R., Kervella, P., Monteiro, H., Sfair, R., El Moutamid, M., Tancredi, G., Spagnotto, J., Maury, A., Morales, N., Gil-Hutton, R., Roland, S., Ceretta, A., Gu, S.H., Wang, X.B., Harpsøe, K., Rabus, M., Manfroid, J., Opitom, C., Vanzi, L., Mehret, L., Lorenzini, L., Schneiter, E.M., Melia, R., Lecacheux, J., Colas, F., Vachier, F., Widemann, T., Almenares, L., Sandness, R.G., Char, F., Perez, V., Lemos, P., Martinez, N., Jørgensen, U.G., Dominik, M., Roig, F., Reichart, D.E., Lacluyze, A.P., Haislip, J.B., Ivarsen, K.M., Moore, J.P., Frank, N.R., Lambas, D.G., 2014. A ring system detected around the Centaur (10199) Chariklo. Nature508, 72–75.

Camargo, J.I.B., Vieira-Martins, R., Assafin, M., Braga-Ribas, F., Sicardy, B., Desmars, J., Andrei, A.H., Benedetti-Rossi, G., Dias-Oliveira, A., 2014. Candidate stellar occultations by Centaurs and trans-Neptunian objects up to 2014. Astron. Astrophys. 561, A37.

Chiang, E.I., Goldreich, P., 2000. Apse Alignment of Narrow Eccentric Planetary Rings. ApJ540, 1084–1090.

Coppejans, R., Gulbis, A.A.S., Kotze, M.M., Coppejans, D.L., Worters, H.L., Woudt, P.A., Whittal, H., Cloete, J., Fourie, P., 2013. Characterizing and Commissioning the Sutherland High-Speed Optical Cameras (SHOC). PASP125, 976.

Cuzzi, J.N., 1985. Rings of Uranus - Not so thick, not so black. Icarus 63, 312–316.

Desmars, J., Camargo, J.I.B., Braga-Ribas, F., Vieira-Martins, R., Assafin, M., Vachier, F., Colas, F., Ortiz, J.L., Duffard, R., Morales, N., Sicardy, B., Gomes-Júnior, A.R., Benedetti-Rossi, G., 2015. Orbit determination of trans-Neptunian objects and Centaurs for the prediction of stellar occultations. Astron. Astrophys. 584, A96.

Duffard, R., Pinilla-Alonso, N., Ortiz, J.L., Alvarez-Candal, A., Sicardy, B., Santos-Sanz, P., Morales, N., Colazo, C., Fernández-Valenzuela, E., Braga-Ribas, F., 2014. Photometric and spectroscopic evidence for a dense ring system around Centaur Chariklo. Astron. Astrophys. 568, A79.

Elliot, J.L., French, R.G., Meech, K.J., Elias, J.H., 1984. Structure of the Uranian rings. I - Square-well model and particle-size constraints. Astron. J. 89, 1587–1603.

Elliot, J.L., Nicholson, P.D., The rings of Uranus. in: IAU Colloq. 75: Planetary Rings, (Eds.) R. Greenberg, A. Brahic 1984 pp. 25–72.

Fitzpatrick, E.L., 1999. Correcting for the Effects of Interstellar Extinction. PASP111, 63–75.

Fornasier, S., Lazzaro, D., Alvarez-Candal, A., Snodgrass, C., Tozzi, G.P., Carvano, J.M., Jiménez-Teja, Y., Silva, J.S., Bramich, D.M., 2014. The Centaur 10199 Chariklo: investigation into rotational period, absolute magnitude, and cometary activity. Astron. Astrophys. 568, L11.

French, R.G., Elliot, J.L., Levine, S.E., 1986. Structure of the Uranian rings. II - Ring orbits and widths. Icarus 67, 134–163.

French, R.G., Nicholson, P.D., Hedman, M.M., Hahn, J.M., McGhee-French, C.A., Colwell, J.E., Marouf, E.A., Rappaport, N.J., 2016. Deciphering the embedded wave in Saturn's Maxwell ringlet. Icarus 279, 62–77.

French, R.G., Nicholson, P.D., Porco, C.C., Marouf, E.A., *Dynamics and structure of the Uranian rings* 1991 pp. 327–409 pp. 327–409.

Gaia Collaboration, Brown, A.G.A., Vallenari, A., Prusti, T., de Bruijne, J.H.J., Mignard, F., Drimmel, R., Babusiaux, C., Bailer-Jones, C.A.L., Bastian, U., et al., 2016. Gaia Data Release 1. Summary of the astrometric, photometric, and survey properties. Astron. Astrophys. 595, A2.

Goldreich, P., Tremaine, S., 1979. Towards a theory for the Uranian rings. Nature 277, 97–99.

Horner, J., Evans, N.W., Bailey, M.E., 2004. Simulations of the population of Centaurs - I. The bulk statistics. Mon. Not. R. Astron. Soc.354, 798–810.

Mosqueira, I., Estrada, P.R., 2002. Apse Alignment of the Uranian Rings. Icarus 158, 545–556.

Ortiz, J.L., Duffard, R., Pinilla-Alonso, N., Alvarez-Candal, A., Santos-Sanz, P., Morales, N., Fernández-Valenzuela, E., Licandro, J., Campo Bagatin, A., Thirouin, A., 2015. Possible ring material around centaur (2060) Chiron. Astron. Astrophys. 576, A18.

Pan, M., Wu, Y., 2016. On the Mass and Origin of Chariklo's Rings. Astron. J. 821, 18.

Press, W.H., Teukolsky, S.A., Vetterling, W.T., Flannery, B.P., *Numerical recipes in FOR-TRAN. The art of scientific computing* 1992.

Roques, F., Moncuquet, M., Sicardy, B., 1987. Stellar occultations by small bodies - Diffraction effects. Astron. J. 93, 1549–1558.

Ruprecht, J.D., Bosh, A.S., Person, M.J., Bianco, F.B., Fulton, B.J., Gulbis, A.A.S., Bus, S.J., Zangari, A.M., 2015. 29 November 2011 stellar occultation by 2060 Chiron: Symmetric jet-like features. Icarus 252, 271–276.

Sicardy, B., Benedetti-Rossi, G., Buie, M.W., Langlois, M., Lellouch, E., Camargo, J.I.B., Braga-Ribas, F., Duffard, R., Ortiz, J.L., Bérard, D., Meza, E., Boccaletti, A., Bockelée-Morvan, D., Dumas, C., Gratadour, D., 2015a. Observations of Chariklo's rings in 2015. European Planetary Science Congress 2015, held 27 September - 2 October, 2015 in Nantes, France, Online at ¡A href="http://meetingorganizer.copernicus.org/EPSC2015/EPSC2015"¿ http://meetingorganizer.copernicus.org/EPSC2015¡/A¿, id.EPSC2015-750 10, EPSC2015–750.

Sicardy, B., Buie, M.W., Benedetti-Rossi, G., Braga-Ribas, F., Bueno de Camargo, J.I., Duffard, R., Ortiz, J.L., Gratadour, D., Dumas, C., Constraints on Chariklo's rings from HST and VLT observations. in: AAS/Division for Planetary Sciences Meeting Abstracts vol. 47 of *AAS/Division for Planetary Sciences Meeting Abstracts* 2015 p. 104.01.

Sicardy, B., El Moutamid, M., Quillen, A.C., Schenk, P.M., Showalter, M.R., Walsh, K., 2016. Rings beyond the giant planets. ArXiv e-prints.

van Belle, G.T., 1999. Predicting Stellar Angular Sizes. PASP111, 1515–1523.

Table 1.   Circumstances of positive detections (main body and/or rings)

Site	Longitude Latitude Altitude (m)	Telescope	Instrument Exposure Time (s)	Observers	Results
Date					

Date
Rmag (NOMAD catalog), (α, δ) star coordinates, $\theta_\star$ stellar diameter[a]
$(\alpha_{Ck}, \delta_{Ck})$ derived Chariklo's geocentric coordinates at specified date

Site	Longitude Latitude Altitude (m)	Telescope	Instrument Exposure Time (s)	Observers	Results

June 3, 2013
$R = 12.070$, $\alpha = 16h56m06.4876s$, $\delta = -40°31'30.205''$, $\theta_\star = 2.18$ km
at 06:25:30 UT: $\alpha_{Ck} = 16h56m06.3202s$, $\delta_{Ck} = -40°31'30.2803''$

See details in Braga-Ribas et al. (2014)

February 16, 2014
$R = 16.$, $\alpha = 17h35m55.3333s$, $\delta = -38°05'17.184''$, $\theta_\star = 0.265$ km
at 07:45:35 UT: $\alpha_{Ck} = 17h35m54.980s$, $\delta_{Ck} = -38°05'17.449''$

Site	Longitude Latitude Altitude (m)	Telescope	Instrument Exposure Time (s)	Observers	Results
Paranal Chile	24 37 31. S 70 24 07.95 W 2635.43	UT4 8.2 m H-filter	HAWK-I 0.25	F. Selman, C. Herrera G. Carraro, S. Brillant C. Dumas, V. D. Ivanov	C1R and C2R partially resolved
San Pedro Atacama Chile	22 57 12.3 S 68 10 47.6 W 2397	50 cm	APOGEE U42 10	A. Maury N. Morales	Main body

March 16, 2014
$R = 15.45$, $\alpha = 17h40m39.8690s$, $\delta = -38°25'46.887''$, $\theta_\star = 0.121$ km
at 20:31:45 UT: $\alpha_{Ck} = 17h40m39.7743s$, $\delta_{Ck} = -38°25'46.4198''$

Site	Longitude Latitude Altitude (m)	Telescope	Instrument Exposure Time (s)	Observers	Results
Doi Inthanon Thailand	18 34 25.41 N 98 28 56.06 E 2450	TNT 2.4 m R'-filter	ULTRASPEC 3.3	P. Irawati A. Richichi	C1R and C2R unresolved

April 29, 2014
$R_A^{(b)} = 12.72$, $\alpha_A^{(b)} = 17h39m02.1336s$, $\delta_A^{(b)} = -38°52'48.801''$, $\theta_{\star A}^{(b)} = 0.199$ km
at 23:14:12 UT: $\alpha_{Ck} = 17h39m01.7943s$, $\delta_{Ck} = -38°52'48.858''$

Site	Longitude Latitude Altitude (m)	Telescope	Instrument Exposure Time (s)	Observers	Results
SAAO Sutherland South Africa	32 22 46.0 S 20 48 38.5 E 1760	1.9 m	SHOC 0.0334	H. Breytenbach A. A. Sickafoose	C1R and C2R resolved Main body
Gifberg South Africa	31 48 34.6 S 18 47 0.978 E 338	30 cm	Raptor Merlin 127 0.047	J.-L. Dauvergne P. Schoenau	Grazing C2R
Springbok South Africa	29 39 40.2 S 17 52 58.8 W 900	30 cm	Raptor Merlin 127 0.06	F. Colas C. de Witt	C1R and C2R sharp and resolved

June 28, 2014
$R = 13.65$, $\alpha = 17h24m50.3821s$, $\delta = -38°41'05.609''$, $\theta_\star = 0.167$ km
at 22:24:35 UT: $\alpha_{Ck} = 17h24m50.2954s$, $\delta_{Ck} = -38°41'05.7445''$

Site	Longitude Latitude Altitude (m)	Telescope	Instrument Exposure Time (s)	Observers	Results
Hakos Namibia	23 14 11 S 16 21 41.5 E 1825	50 cm AK3	Raptor Merlin 127 0.2	K.-L. Bath	C1R and C2R unresolved
Kalahari South Africa	26 46 26.91 S 20 37 54.258 E	30 cm	Raptor Merlin 127 0.4	L. Maquet	Main body

Table 1—Continued

Site	Longitude Latitude Altitude (m)	Telescope	Instrument Exposure Time (s)	Observers	Results
	Date Rmag (NOMAD catalog), (α, δ) star coordinates, $\theta_\star$ stellar diameter[a] $(\alpha_{Ck}, \delta_{Ck})$ derived Chariklo's geocentric coordinates at specified date				
Twee Rivieren South Africa	861 26 28 14.106 S 20 36 41.694 E 883	30 cm	Raptor Merlin 127 0.4	J.-L. Dauvergne	Main body
	April 26, 2015 $R = 12.04$, $\alpha = 18h10m46.1450s$, $\delta = -36°38'56.368''$, $\theta_\star = 0.361$ km at 02:11:58 UT: $\alpha_{Ck} = 18h10m45.9676s$, $\delta_{Ck} = -36°38'56.608''$				
Los Molinos Uruguay	34 45 19.3 S 56 11 24.6 W 130	OALM 46 cm	FLI CCD 0.8	S. Roland R. Salvo G. Tancredi	CR and C2R unresolved
	May 12, 2015 $R = 15.93$, $\alpha = 18h08m29.2962s$, $\delta = -36°44'56.814''$, $\theta_\star = 0.219$ km at 17:55:40 UT: $\alpha_{Ck} = 18h08m29.2447s$, $\delta_{Ck} = -36°44'56.7965''$				
Samford Valley Australia	27 22 07.00 S 152 50 53.00 E 80	35 cm	G-star 0.32	J. Bradshaw	Main Body Emersion of unresolved rings only
	July 25, 2016 $R = 14.02$, $\alpha = 18h20m35.3645s$, $\delta = -34°02'29.590''$, $\theta_\star = 0.234$ km at 23:59:00 UT: $\alpha_{Ck} = 18h20m35.3640s$, $\delta_{Ck} = -34°02'29.0378''$				
Liverpool Telescope Canary Islands	28 45 44.8 N 17 52 45.2 W 2363	2 m	RISE 0.6	J.-L. Ortiz N. Morales	Main Body
	August 08, 2016 $R = 13.67$, $\alpha = 18h18m03.6927s$, $\delta = -33°52'28.392''$, $\theta_\star = 0.204$ km at 19:57:00 UT: $\alpha_{Ck} = 18h18m03.8297s$, $\delta_{Ck} = -33°52'28.181''$ or $\alpha_{Ck} = 18h18m03.8449s$, $\delta_{Ck} = -33°52'28.196''$				
Windhoek (CHMO) Namibia	22 41 54.5 S 17 06 32.0 E 1920	35 cm	ZWO / ASI120MM 1	H.-J. Bode	Main Body C1R and C2R unresolved
	August 10, 2016 $R = 16.53$, $\alpha = 18h17m47.3492s$, $\delta = -33°51'02.516''$, $\theta_\star = 0.053$ km at 14:23:00 UT: $\alpha_{Ck} = 18h17m47.3089s$, $\delta_{Ck} = -33°51'02.478''$				
Murrumbateran Australia	34 57 31.50 S 148 59 54.80 E 594	40 cm	WATEC 910BD 0.64	D. Herald	Main Body
	August 10, 2016 $R = 16.22$, $\alpha = 18h17m46.4827s$, $\delta = -33°50'57.826''$, $\theta_\star = 0.083$ km at 16:43:00 UT: $\alpha_{Ck} = 18h17m46.4457s$, $\delta_{Ck} = -33°50'57.523''$				
Les Makes La Réunion	21 11 57.4 S 55 24 34.5 E 972	60 cm	Raptor Merlin 127 2	F. Vachier	Main Body

Table 1—Continued

Site	Longitude Latitude Altitude (m)	Telescope	Instrument Exposure Time (s)	Observers	Results
Date Rmag (NOMAD catalog), (α, δ) star coordinates, $\theta_\star$ stellar diameter[a] $(\alpha_{Ck}, \delta_{Ck})$ derived Chariklo's geocentric coordinates at specified date				

Site	Longitude Latitude Altitude (m)	Telescope	Instrument Exposure Time (s)	Observers	Results
August 15, 2016 $R = 14.64$, $\alpha = $ 18h17m06.2228s, $\delta = -33°46'56.315''$, $\theta_\star = 0.103$ km at 11:38:00 UT: $\alpha_{Ck} = $ 18h17m06.1638s, $\delta_{Ck} = -33°46'56.513''$				
Darfield New Zealand	43 28 52.90 S 172 06 24.40 E 210	25 cm	WATEC 910 BD 2.56	B. Loader	Main Body
October 1, 2016 $R = 15.36$, $\alpha = $ 18h16m20.0796s, $\delta = -33°01'10.756''$, $\theta_\star = 0.119$ km at 10:10:00 UT: $\alpha_{Ck} = $ 18h16m20.0324s, $\delta_{Ck} = -33°01'10.841''$				
Rockhampton Australia	23 16 09.00 S 150 30 00 E 50	30 cm	WATEC 910BD 0.320	S. Kerr	Main Body C1R and C2R unresolved
Adelaide Heights School Australia	34 48 44.701 S 138 40 56.899 E 167	30 cm	QHY 5L11 1	A. Cool B. Lade	Main body C1R and C2R unresolved

[a] projected at Chariklo's distance (using van Belle 1999, except for the April 29, 2014, see text for details).
[b] The index A refers to the primary of the binary star.

Table 2. Circumstances of observations that detected no event or during which no data was acquired

Site	Longitude Latitude Altitude (m)	Telescope	Instrument Exposure Time (s)	Observers
February 16, 2014				
Cerro Tololo Chile	30 10 03.36 S 70 48 19.01 W 2207	0.4 m 4 telescopes	PROMPT 6.0/2.0	J. Pollock
La Silla Chile	29 15 16.59 S 70 44 21.82 W 2315	TRAPPIST 60 cm	FLI PL3041-BB 4.5	E. Jehin
La Silla Chile	29 15 32.1 S 70 44 01.5 W 2375	NTT 3.55 m H-filter	SOFI 0.05	L. Monaco + visitor team
April 29, 2014				
Hakos Namibia	23 14 50.4 S 16 21 41.5 E 1825	50 cm AK3	Raptor Merlin 127 0.075	K.-L. Bath
Hakos Namibia	23 14 50.4 S 16 21 41.5 E 1825	50 cm RC50	i-Nova 1.	R. Prager
Windhoek (CHMO) Namibia	22 41 54.5 S 17 06 32.0 E 1920	35 cm	Raptor Merlin 127 0.1	W. Beisker
June 28, 2014				
Les Makes La Réunion	21 11 57.4 S 55 24 34.5 E 972	60 cm	WATEC 910HX 0.4	A. Peyrot J-P. Teng
April 26, 2015				
Bigand Provincia Santa Fé Argentina	33 26 11 S 61 08 24 W 90	15 cm	Canon Ti 5	S. Bilios
Bigand Provincia Santa Fé Argentina	33 26 11 S 61 08 24 W 90	15 cm	Canon EOS 3.2	J. Nardon
La Silla Chile	29 15 16.6 S 70 44 21.8 W 2315	TRAPPIST 60 cm	FLI PL3041-BB 4.5	E. Jehin
Bosque Alegre Argentina	31 35 54.0 S 64 32 58.7 W 1250	76 cm	QHY6 1.2	R. Melia C. Colazo
Santa Rosa Argentina	36 38 16 S 64 19 28 W 182	20 cm	Meade DSI-I 3	J. Spagnotto
Santa Martina Chile	33 16 09.0 S 70 32 04.0 W 1450	40 cm	Raptor Merlin 127 0.5	R. Leiva Espinoza
Buenos Aires (AAAA) Argentina	34 36 16.94 S 58 26 04.37 W 0	25 cm	ST9e 4	A. Blain

Table 2—Continued

Site	Longitude Latitude Altitude (m)	Telescope	Instrument Exposure Time (s)	Observers
May 12, 2015				
Reedy Creek Australia	28 06 30.4 S 153 23 52.90 E 66	25 cm	WATEC 120N+ 0.64	J. Broughton
July 25, 2016				
Granada Spain	37 00 38.49 N 03 42 51.39 W 1043	60 cm	Raptor Merlin 127 0.4	S. Alonso A. Román
Albox Spain	37 24 20.0 N 02 09 6.5 E 493	40 cm	Atik 314L+ 3	J.-L. Maestre
August 10, 2016 - 14h UT				
Blue Mountains Australia	33 39 51.9 S 150 38 27.9 E 286	30 cm	WATEC 910BD 5.12	D. Gault
Samford Valley Australia	27 22 07.00 S 152 50 53.00 E 80	35 cm	WATEC 910BD 0.64	J. Bradshaw
Rockhampton Australia	23 16 09.00 S 150 30 00.00 E 50	30 cm	WATEC 910BD 1.28	S. Kerr
Dunedin New Zealand	45 52 20.83 S 170 29 29.90 E 154	36 cm	Raptor Merlin 127 2.	F. Colas A. Pennell P.-D. Jaquiery
Sydney Australia	33 48 35.04 S 150 46 36.90 E 37	36 cm	Raptor Merlin 127 2.2	H. Pavlov
August 15, 2016				
Canberra Australia	35 11 55.30 S 149 02 57.50 E 610	40 cm	WATEC 910BD 2.56	J. Newman
Murrumbateran Australia	34 57 31.50 S 148 59 54.80 E 594	40 cm	WATEC 920BD 0.32	D. Herald
Greenhill Observatory Tasmania	42 25 51.8 S 147 17 15.8 E 641	1.3 m	Raptor Merlin 127 0.5	K. Hill A. Cole
Rockhampton Australia	23 16 09.00 S 150 30 00.00 E 50	30 cm	WATEC 910BD 1.28	S. Kerr
Linden Observatory Australia	33 42 27.3 S 150 29 43.5 E 574	76 cm	Grasshopper Express with ADVS 0.533	D. Gault R. Horvat R.A. Paton L. Davis

Table 2—Continued

Site	Longitude Latitude Altitude (m)	Telescope	Instrument Exposure Time (s)	Observers
WSU Penrith Observatory Sydney Australia	33 45 43.31 S 150 44 30.30 E 60	62 cm	Raptor Merlin 127 2	H. Pavlov D. Giles D. Maybour M. Barry
October 1, 2016				
Blue Mountains Australia	33 39 51.9 S 150 38 27.9 E 286	30 cm	WATEC 910BD 0.64	D. Gault
Linden Observatory Australia	33 42 27.3 S 150 29 43.5 E 574	76 cm	Grasshopper Express with ADVS 0.27	M. Barry
Miles Australia	26 39 20.52 S 150 10 19.44 E 277	25 cm	WATEC 120N+ 0.64	D. Dunham J. Dunham
Reedy Creek Australia	28 06 30.4 S 153 23 52.90 E 66	25 cm	WATEC 120N+ 1.28	J. Broughton
Samford Valley Australia	27 22 07.00 S 152 50 53.00 E 80	35 cm	WATEC 910BD 0.16	J. Bradshaw

The following stations were cloudy or had technical failure, no data were acquired:

February 16, 2014: Santa Martina (Chile), Bosque Alegre (Argentina)

April 29, 2014 : Rodrigues, Sainte Marie, Les Makes (La Réunion) ; Calitzdorp and LCOGT (South Africa)

April 26, 2015 : Cerro Tololo (Chile)

July 25, 2016: TRAPPIST Nord (Marocco), TAD (Canary Islands), Teide Observatory (Canary Islands)

August 8, 2016 : Les Makes (La Réunion)

August 15, 2016: Mount John Observatory, Dunedin, Bootes-3, Wellington (New Zealand)

October 1, 2016: Murrumbateran, Canberra (Australia)

Table 3: Sharpness of C1R edges, Δw_r, from April 29, 2014 events

Event	Inner edge (km)	Outer edge (km)
	(1σ level)	
Springbok Ingress	1.1	1.1
Springbok Egress	1.2	1.5
SAAO Ingress	0.6	0.9
SAAO Egress	0.8	0.4

Table 4. Ring occultation timings and derived physical parameters (resolved events)

Date	Event	t_0 UT[a]	$v_\perp^{[b]}$ (km/s)	$v_r^{[b]}$ (km/s)	$L^{[c]}$ (deg.)	$W_r^{[d]}$ (km)	$E_p^{[e]}$ (km)	$p_N^{[e]}$
		C1R						
Jun 3, 2013	Danish ingress[f]	$06:25:21.166\pm0.0007$	20.345	36.113	341.76	6.16 ± 0.11	1.90 ± 0.022	0.308 ± 0.003
	Danish egress[f]	$06:25:40.462\pm0.0012$	22.031	36.504	124.38	7.14 ± 0.04	1.73 ± 0.023	0.24 ± 0.004
Feb 16, 2014	VLT ingress	$07:45:25.541^{+0.010}_{-0.004}$	19.532	28.794	183.37	$5.316^{+0.868}_{-1.916}$	$1.996^{+0.092}_{-0.031}$	$0.375^{+0.125}_{-0.025}$
	VLT egress	$07:45:45.133^{+0.313}_{-0.332}$	21.293	29.602	300.99	$4.833^{+1.667}_{-0.476}$	$2.04^{+0.36}_{-0.14}$	$0.443^{+0.078}_{-0.103}$
Apr 29, 2014	Springbok ingress	$23:14:25.884\pm0.007$	13.432	16.493	287.42	5.575 ± 0.398	$1.80^{+0.122}_{-0.143}$	$0.3125^{+0.024}_{-0.027}$
	Springbok egress	$23:15:04.362\pm0.006$	10.720	16.655	157.83	$6.75^{+0.48}_{-0.21}$	$2.595^{+0.148}_{-0.166}$	$0.33^{+0.017}_{-0.033}$
	SAAO ingress	$23:13:56.191\pm0.007$	12.756	13.895	266.656	5.68 ± 0.2	$1.88^{+0.22}_{-0.12}$	$0.32^{+0.037}_{-0.021}$
	SAAO egress	$23:14:28.964\pm0.008$	9.260	14.249	198.899	6.625 ± 0.2	$1.695^{+0.175}_{-0.115}$	$0.241^{+0.024}_{-0.022}$
		C2R						
Jun 3, 2013	Danish ingress[f]	$06:25:20.765\pm0.011$	20.412	36.283	341.76	$3.380^{+1.424}_{-1.797}$	0.168 ± 0.02	$0.05^{+0.05}_{-0.01}$
	Danish egress[f]	$06:25:40.847\pm0.006$	22.029	36.632	124.38	$3.231^{+0.899}_{-1.124}$	0.228 ± 0.02	$0.07^{+0.03}_{-0.01}$
Feb 16, 2014	VLT ingress	$07:45:25.285^{+0.057}_{-0.033}$	19.532	28.794	183.37	$5.053^{+1.000}_{-2.385}$	$0.491^{+0.445}_{-0.227}$	$0.091^{+0.495}_{-0.00}$
	VLT egress	$07:45:45.473^{+0.037}_{-0.053}$	21.293	29.602	300.99	$3.333^{+1.667}_{-1.333}$	$0.522^{+0.078}_{-0.050}$	$0.119^{+0.609}_{-0.118}$
Apr 29, 2014	Springbok ingress	$23:14:24.990\pm0.020$	13.430	16.460	287.42	$0.34^{+1.37}_{-0.24}$	$0.125^{+0.076}_{-0.064}$	$0.368^{+0.632}_{-0.288}$
	Springbok egress	$23:15:5.324\pm0.019$	10.722	16.620	157.832	$0.6^{+1.7}_{-0.1}$	$0.253^{+0.079}_{-0.069}$	$0.582^{+0.32}_{-0.45}$
	Gifberg ingress[g]	$23:14:30.109^{+0.015}_{-0.008}$	[g]	[g]	227.190	$0.522^{+0.227}_{-0.399}$	$0.090^{+0.039}_{-0.000}$	$0.186^{+0.814}_{-0.043}$
	Gifberg egress[g]	$23:14:33.750\pm0.008$	[g]	[g]	217.761	$0.181^{+0.008}_{-0.091}$	$0.129^{+0.000}_{-0.039}$	$0.814^{+0.186}_{-0.671}$

[a] t_0 is the mid-time of the event in hours:min:sec. The error bars quoted are given at 1σ level.

[b] $v_\perp$ and v_r are respectively the perpendicular velocity in the sky plane and the radial velocity in the ring plane.

[c] L is the true longitude counted from the J2000 ring plane ascending node.

[d] W_r is the radial width, measured in the plane of the rings.

[e] E_p is the equivalent width: $E_p = W_r \cdot p_N$ where p_N is the normal opacity in the plane of the rings.

[f] Timings given by Braga-Ribas et al. (2014).

[g] As the occultation was grazing, the velocity changes consequently between ingress and egress and to give fixed values is not relevant in this case (see text section 3.2)

Table 5. Ring occultation timings and derived physical parameters (unresolved events)

Date	Event	t_0 UT[†]	$v_\perp$(km/s)[†]	v_r (km/s)[†]	L(deg)[†]	E_p (km)[†]
June 3, 2013	Iguacu ingress	06:24:17.5±1.7[a]	18.059	28.899	2.44	$7.602^{+2.198}_{-5.195}$
	Iguacu egress	06:24:34.1±2.0[a]	21.246	30.446	104.20	$2.580^{+3.712}_{-1.713}$
	Bosque Alegre 154 egress	06:25:11.44±0.14[a]	18.889	32.663	176.11	$3.806^{+1.199}_{-2.198}$
	Ponta Grossa ingress	06:23:58.6±2.5[a]	19.781	34.398	348.04	$9.600^{+0.400}_{-4.795}$
	Ponta Grossa egress	06:24:18.0±2.5[a]	21.965	35.520	120.30	$4.605^{+3.596}_{-3.340}$
	PROMPT ingress	06:25:20.0.46±0.011[a]	21.373	38.269	326.56	$2.208^{+3.196}_{-0.200}$
	Santa Martina ingress	06:25:21.03±0.29[a]	17.556	18.537	264.53	$2.208^{+2.997}_{-0.200}$
	Santa Martina egress	06:25:31.811±0.025[a]	14.605	22.124	200.07	$2.408^{+5.394}_{-0.200}$
	SOAR ingress	06:25:18.8±1.3[a]	21.444	38.320	325.16	$2.208^{+4.196}_{-0.400}$
	SOAR egress	06:25:38.4±1.4[a]	21.660	38.310	140.37	$5.205^{+0.799}_{-3.596}$
	Bosque Alegre C11 ingress	06:24.55.45±1.85[a]	21.522	30.340	287.37	$4.206^{+3.297}_{-2.597}$
	Bosque Alegre C11 egress	06:25:09.45±1.75[a]	17.882	30.062	183.50	$4.206^{+3.396}_{-2.597}$
	TRAPPIST ingress	06:25:20.9±1.9[a]	20.293	36.229	341.31	$4.605^{+3.796}_{-2.198}$
March 16, 2014	Thailand ingress	20:31:37.640±1.33	3.656	3.821	95.06	$1.856^{+0.948}_{-1.197}$
	Thailand egress	20:31:53.885±0.175	3.990	4.290	60.85	$1.856^{+0.150}_{-0.801}$
June 28, 2014	Hakos ingress	22:24:25.796±0.041	19.127	28.619	5.064	$1.472^{+0.455}_{-0.517}$
	Hakos egress	22:24:44.218±0.035	20.971	29.744	117.061	$1.983^{+0.598}_{-0.508}$
April 26, 2015	Los Molinos ingress	02:11:45.707±0.058	3.503	3.513	238.857	$2.914^{+0.151}_{-0.149}$
	Los Molinos egress	02:12:09.195±0.070	2.957	3.989	199.749	$2.400^{+0.28}_{-0.320}$
May 12, 2015	Brisbane egress	17:55:56.823±0.012	11.823	16.567	357.23	$2.707^{+2.398}_{-1.198}$
Aug 8, 2016	Windhoek (CHMO) ingress	19:57:18.209 ± 0.249	15.920	21.878	332.963[b]	$2.043^{+2.762}_{-0.734}$
	Windhoek (CHMO) egress	19:57:51.870 ± 0.382	15.216	21.950	180.196[b]	$3.806^{+2.598}_{-2.297}$
Oct 1, 2016	Rockhampton ingress	10:12:26.284 ± 0.072	10.795	13.121	123.960	$2.523^{+3.481}_{-0.615}$
	Rockhampton egress	10:13:22.928 ± 0.049	12.573	13.146	278.911	$2.586^{+3.818}_{-0.778}$
	Adelaide ingress	10:10:19.826± 0.186	12.421	12.597	91.347	$1.867^{+4.073}_{-0.539}$
	Adelaide egress	10:11:14.558 ± 0.218	9.942	12.651	311.914	$2.047^{+3.534}_{-0.719}$

[†]Same parameters as Table 4

[a]Timings given by Braga-Ribas et al. (2014).

[b]Two geometries are possible for this occultation. We choose arbitrary the closest to the prediction. The other geometry provides different longitudes: $L_{ingress} = 0.154$ and $L_{egress} = 152.948$

Table 6.   Occultation timings for the main body.

Date	Event	$t_{ingress}$ UT	t_{egress} UT
June 3, 2013	Danish	06:25:27.861±0.014	06:25:33.188±0.014
	PROMPT	06:25:24.835±0.009	06:25:35.402±0.015
	TRAPPIST	06:25:27.893±0.019	06:25:33.155±0.007
	SOAR	06:25:24.34±0.59	06:25:34.597±0.009
February 16, 2014	San Pedro de Atacama	07:45:27.450±0.6	07:45:31.125±0.57
June 28, 2014	Kalahari	22:24:07.383±0.126	22:24:14.854±0.096
	Twee Rivieren	22:24:06.689±0.093	22:24:16.481±0.105
April 29, 2014	Springbok	23:14:30.02±0.075	23:14:48.03±0.075
May 12, 2015	Brisbane	17:55:35.530±0.010	17:55:44.135±0.075
July 25, 2016	Liverpool Telescope	23:59:05.494 ±0.054	23:59:12.310 ± 0.054
August 8, 2016	Windhoek (CHMO)	19:57:28.469 ± 0.042	19:57:41.886 ± 0.045
August 10, 2016 - 14h UT	Murrumbateran	14:18:35.030 ± 0.3	14:18:45.145 ± 0.125
August 10, 2016 - 16h UT	Les Makes	16:42:51.305 ± 0.530	16:43:07.917 ± 0.848
August 15, 2016	Darfield	11:38:27.465 ± 0.385	11:38:38.019 ± 0.873
October 1, 2016	Rockhampton	10:12:44.664 ± 0.041	10:13:03.199 ± 0.051
	Adelaide	10:10:41.818 ± 0.118	10:10:54.102 ± 0.064

The error bars quoted are given at 1σ level.
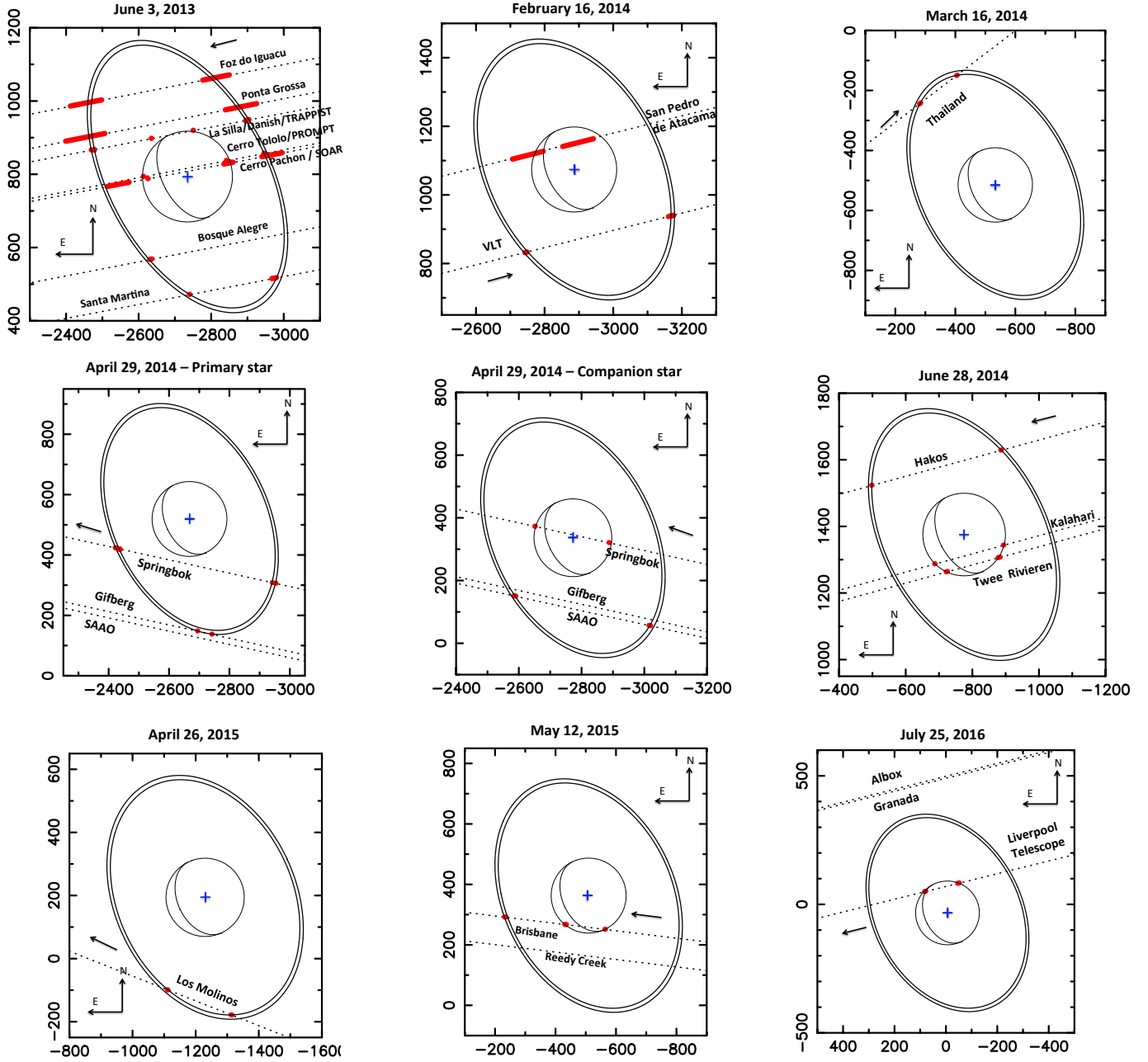
Fig. 1.— Reconstructed geometries of the occultations. The dotted lines are the trajectories of the occulted star relative to Chariklo in the plane of sky as seen from each station (the arrow indicates the direction of the apparent movement of the star). The red segments are the 1σ level error bars on each chord extremity, derived from the corresponding error bars on timings (see Table 4, 5 and 6). For those plots, we use the pole position and the radii from Braga-Ribas et al. (2014): $r_{C1R} = 390.6$ km, $r_{C2R} = 404.8$ km and $r_{Ck} = 124$ km. The center of ring system (blue cross) in each panel represents the offset in right ascension and declination between the predicted and observed positions of the Chariklo relative to the occulted star, as given in Table 1. This offset was used to improve Chariklo's ephemeris.
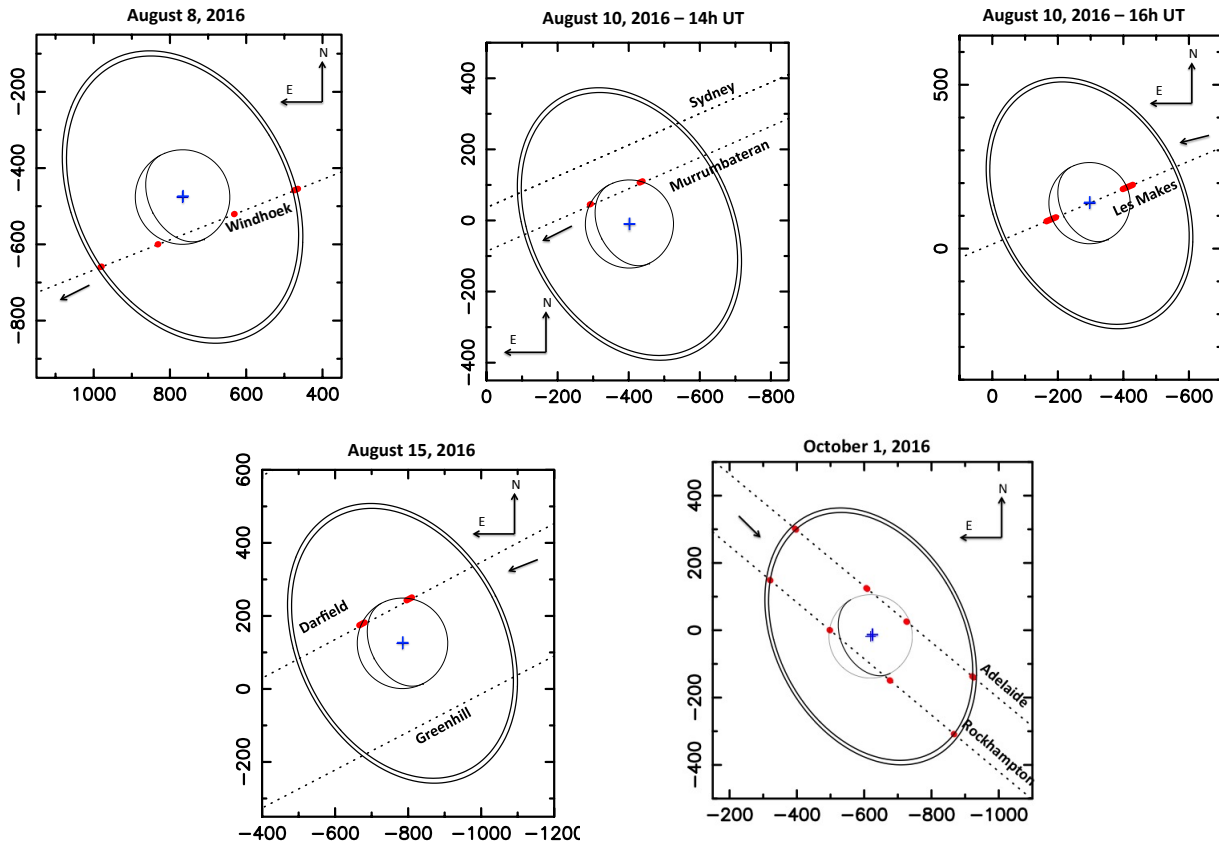
Fig. 2.— Following Figure 1
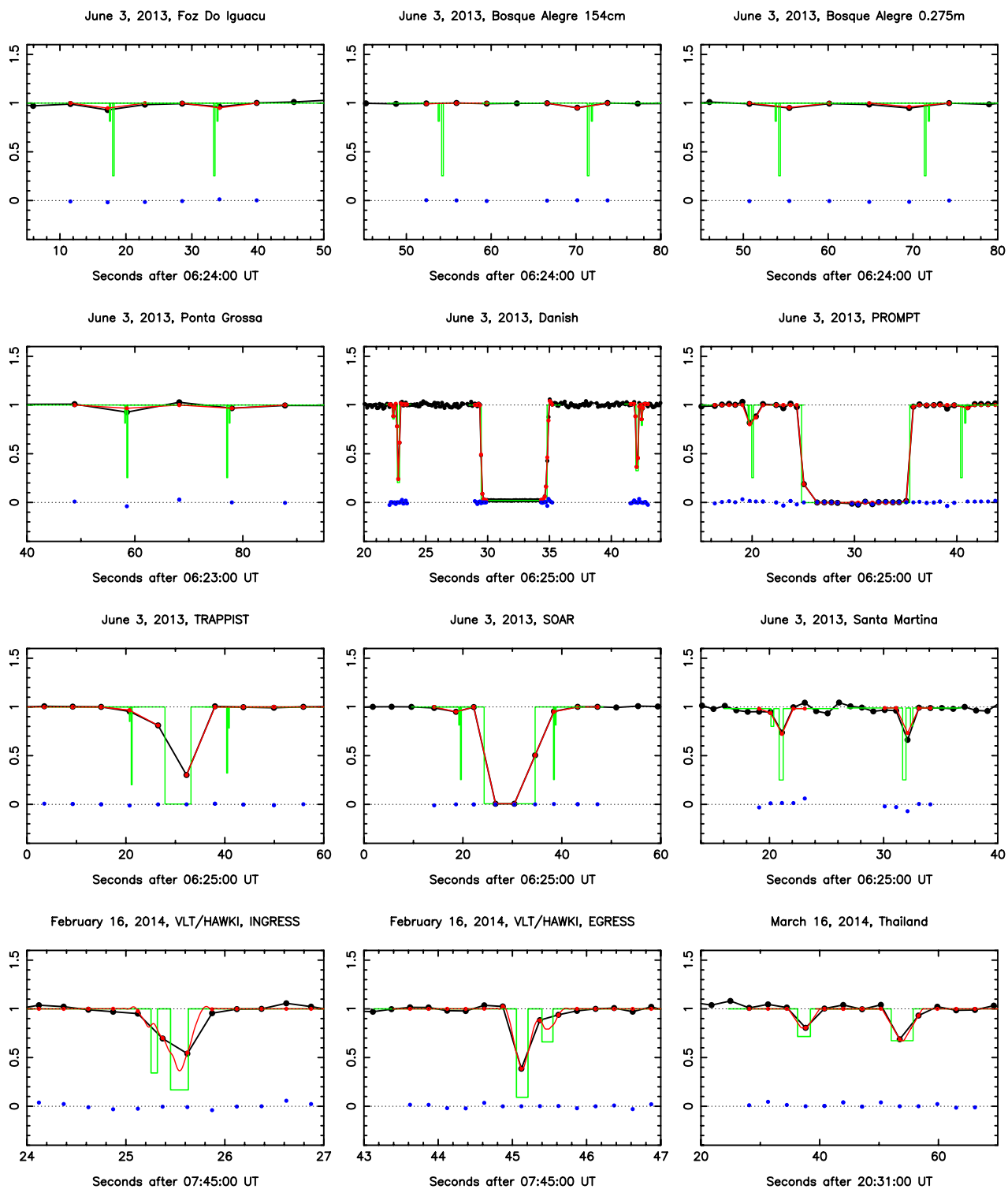
Fig. 3.— Best fits to ring and main body occultations. The black dots are the data points of the light curves (vertical axis represents the normalized flux). They are normalized between zero and unity. The latter corresponding to the full flux from Chariklo and the star occulted. The dotted lines correspond to the zero-level of the occulted star. The green curves are the best fitting square-well models used to generate the synthetic profiles, plotted in red. The physical characteristics of the rings extracted from these plots are listed in Tables 4 and 5. The blue dots are the residual between the synthetic light curves and the data at each data point. Figure 4 shows the fits of remaining rings occultations.
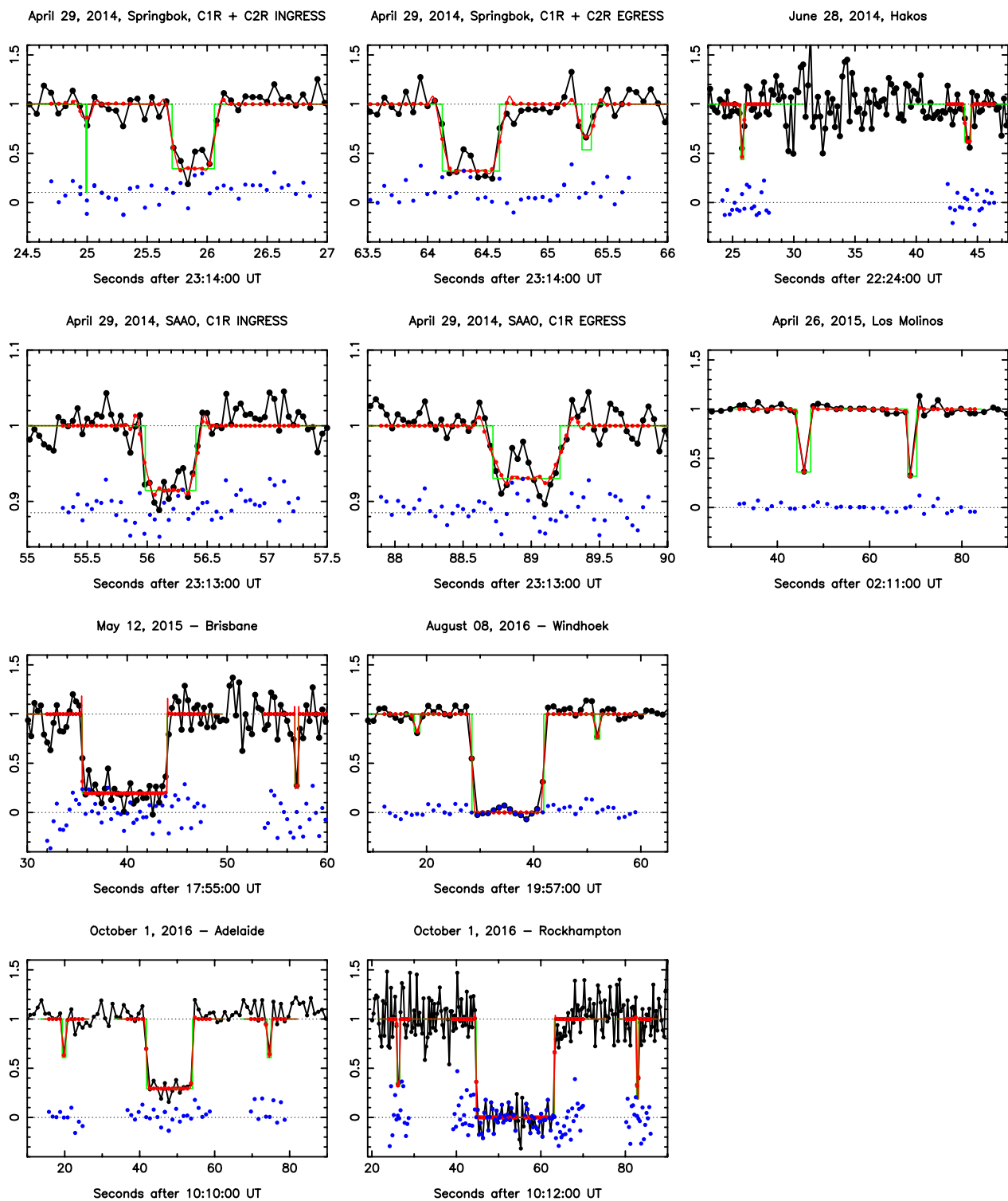
Fig. 4.— Best fits to ring and main body occultations (following and completing Fig. 3). Same legend as in Figure 3, except in the case of the occultation on April 29, 2014 where two stars were occulted. In this case unity corresponds to the flux of the two stars and Chariklo. As SAAO observed an occultation of a secondary star (see Section 2.4), its vertical scale is different from other light curves, for better viewing.
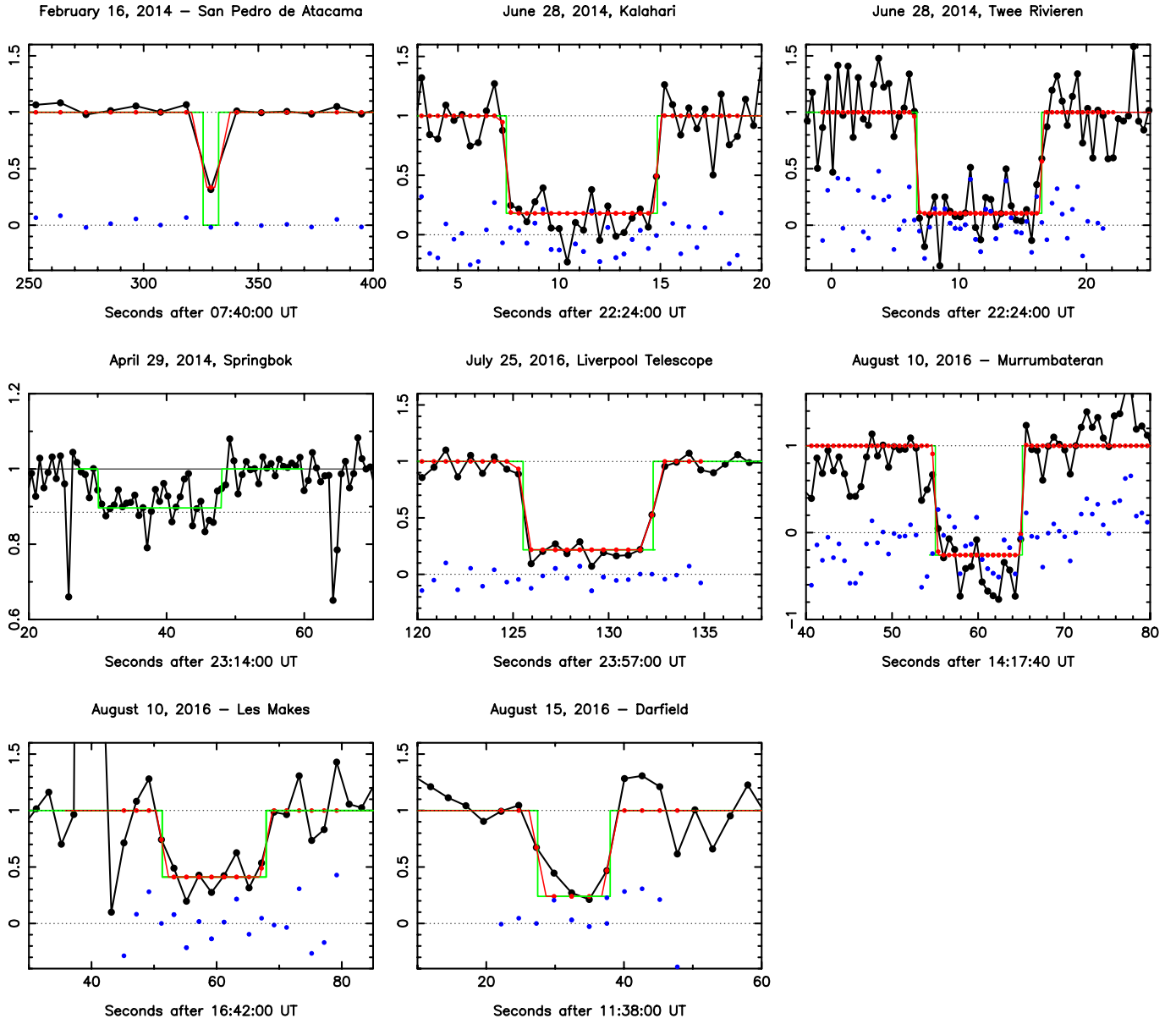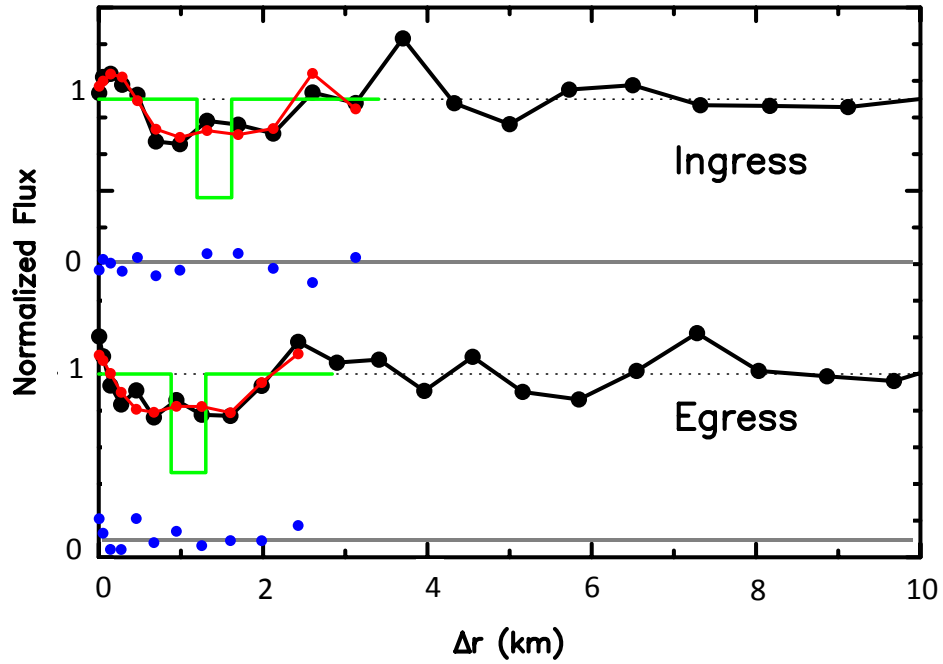
Fig. 5.— Same as Figure 3, but for events with only main body detections.

Fig. 6.— Fits to grazing event in Gifberg (April 29, 2014) using a common width ($W_\perp$ = 0.422 km and $p' = 0.4$) for both rings into 1σ level (see Table 4). The star motion relative to C2R was grazing, so that its velocity perpendicular to the ring changed significantly during the occultation. In this case, it is therefore necessary to express the flux against the distance to the point of closest approach to Chariklo's center in km in the sky plane, Δr. Other than that, color conventions and vertical axis are the same as in Fig. 3.
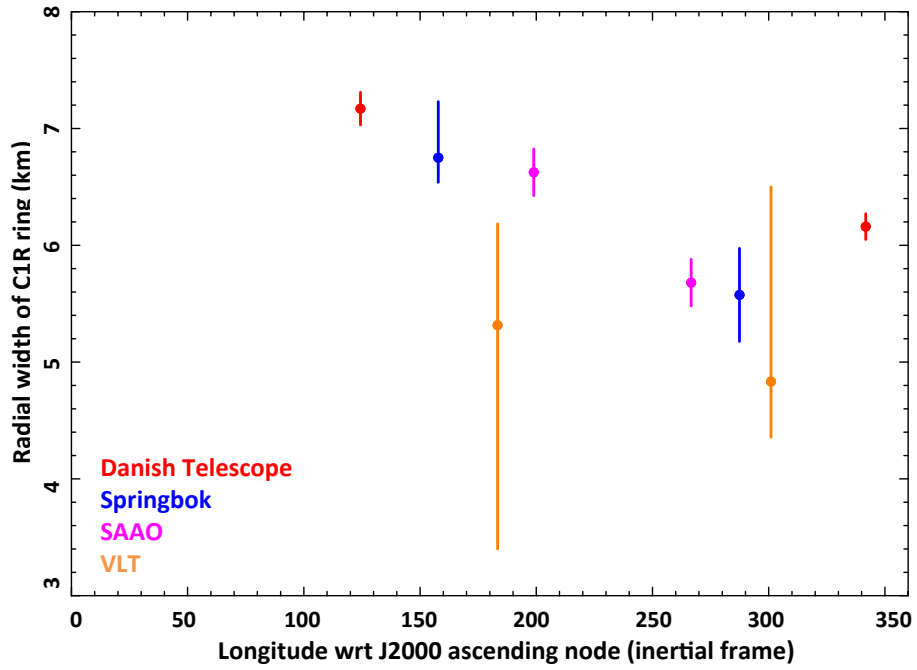
Fig. 7.— Variation of C1R radial width (and 1σ error bars) with true longitude L counted from the J2000 ring plane ascending node for resolved events.
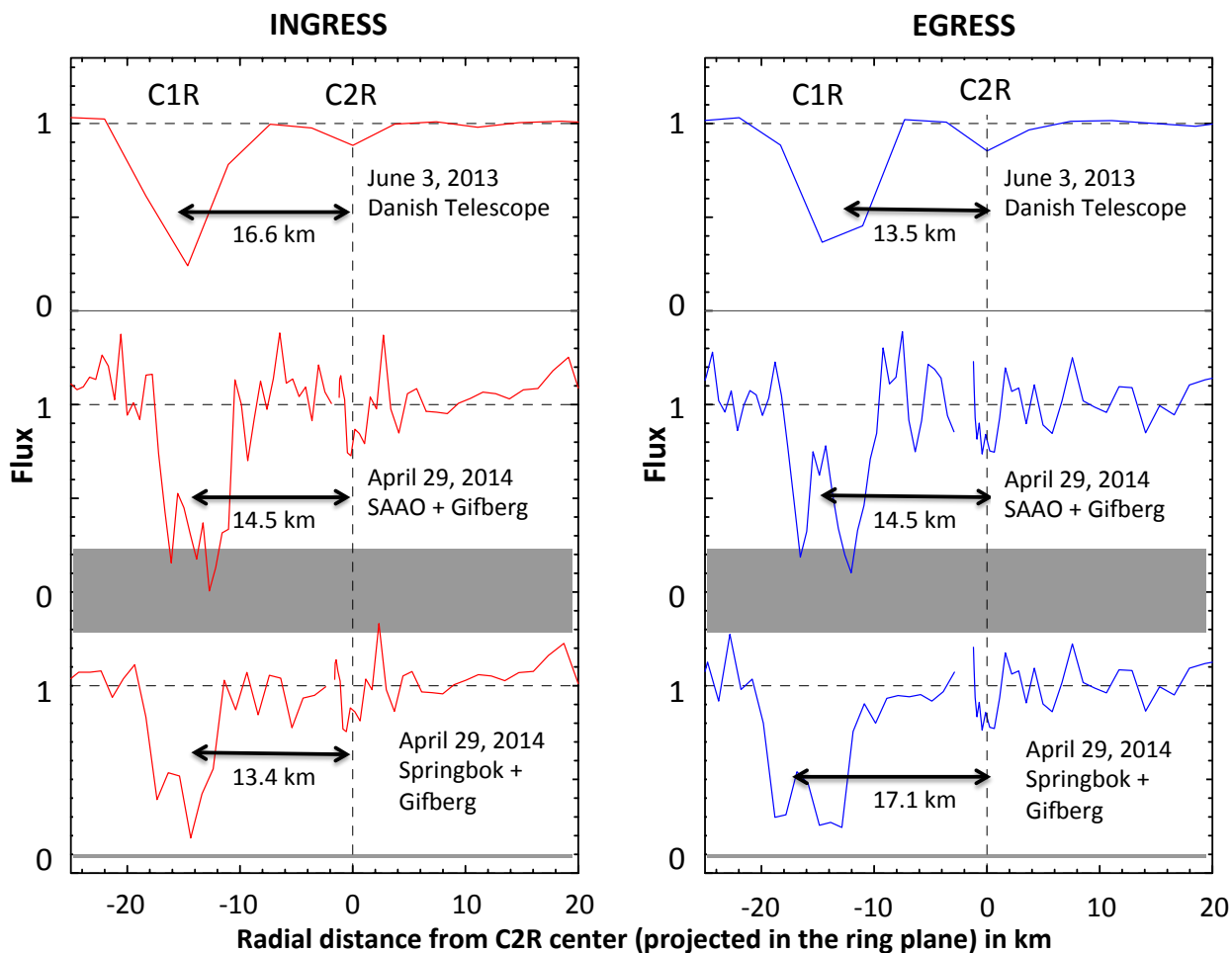
Fig. 8.— Best radial profiles of rings C1R and C2R. The profiles have been plotted arbitrarily against the radial distance (in the ring plane) to the center of the C2R profile, using the pole position of Braga-Ribas et al. (2014). This choice enhances possible changes in the relative distances of the two rings, due for instance to eccentricities of C1R and/or C2R. The horizontal dashed lines correspond to the unocculted star + Chariklo flux. The horizontal gray boxes correspond to the respective zero stellar fluxes. The thickness of a gray box indicates the uncertainty of the photometric calibrations, see text for details (Section 2.4). The left (resp. right) panel corresponds to ingress (resp. egress). Top panels: the June 3, 2013 profiles from the Danish Telescope. Middle and bottom panels: montages constructed from the April 29, 2014 event. The Gifberg profiles showing C2R have been combined with SAAO light curve (middle panel) and Springbok light curve (bottom panel).
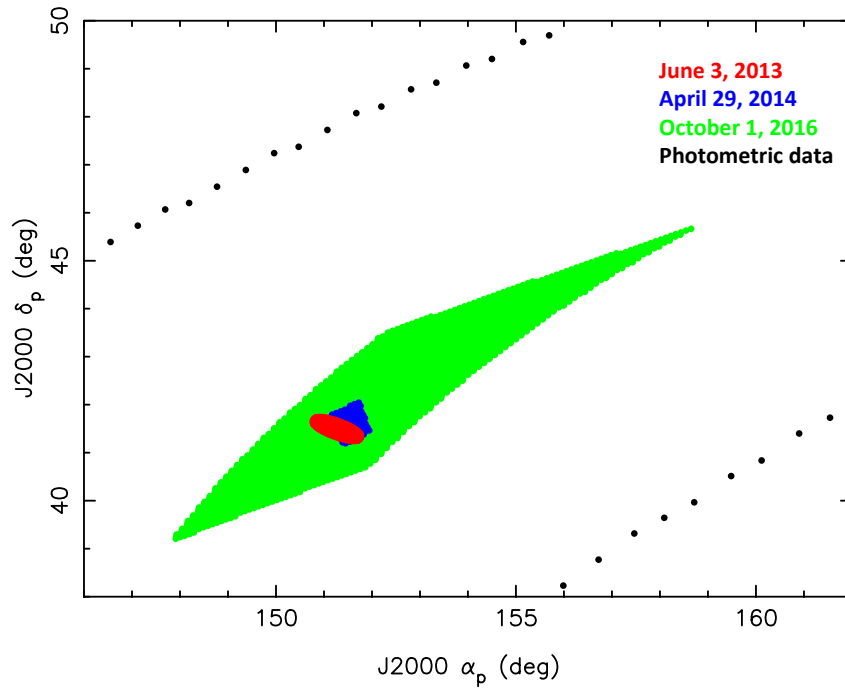
Fig. 9.— Constraints on ring pole. The uncertainty domains (1σ level) on the pole position (α_p, δ_p) for the event on June 3, 2013, April 29, 2014 and October 1, 2016 are plotted in red, blue and green, respectively. The black dots outline the uncertainty domain derived from the long term variations in Chariklo's photometry (Duffard et al. 2014).
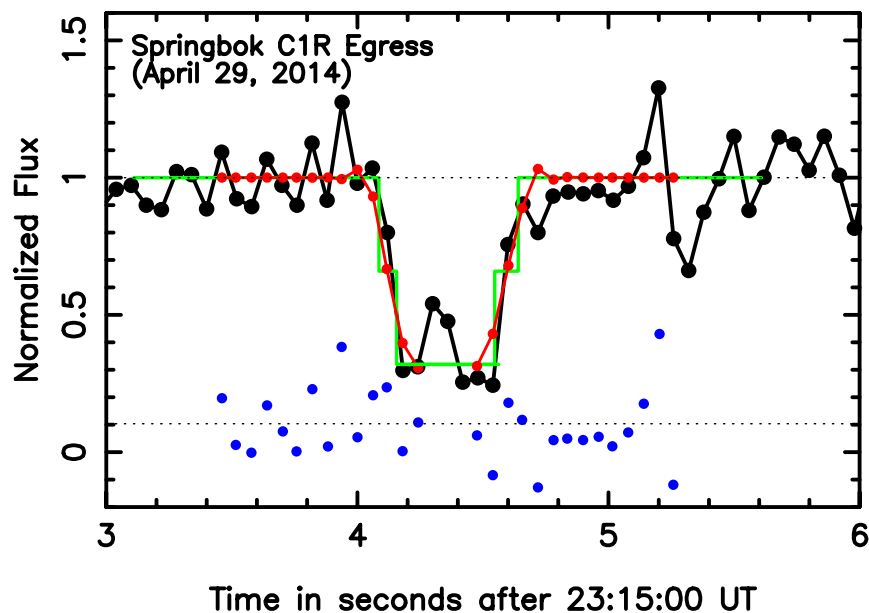
Fig. 10.— Measurement of C1R's edges sharpnesses with an example taken from the Springbok egress profile (April 29, 2014). The green line is the step-wise model of width Δw_r described in Section 3.5. The red dots are the resulting synthetic points (the blue dots showing the residuals). The sharpness parameters Δw_r shown here are the maximum values that are compatible with the data at the 1σ level, with values $\Delta w_r = 1.2$ km for the left (inner) edge and $\Delta w_r = 1.5$ km for the right (outer) edge. Table 3 lists the values of Δw_r obtained with the other resolved C1R profiles.
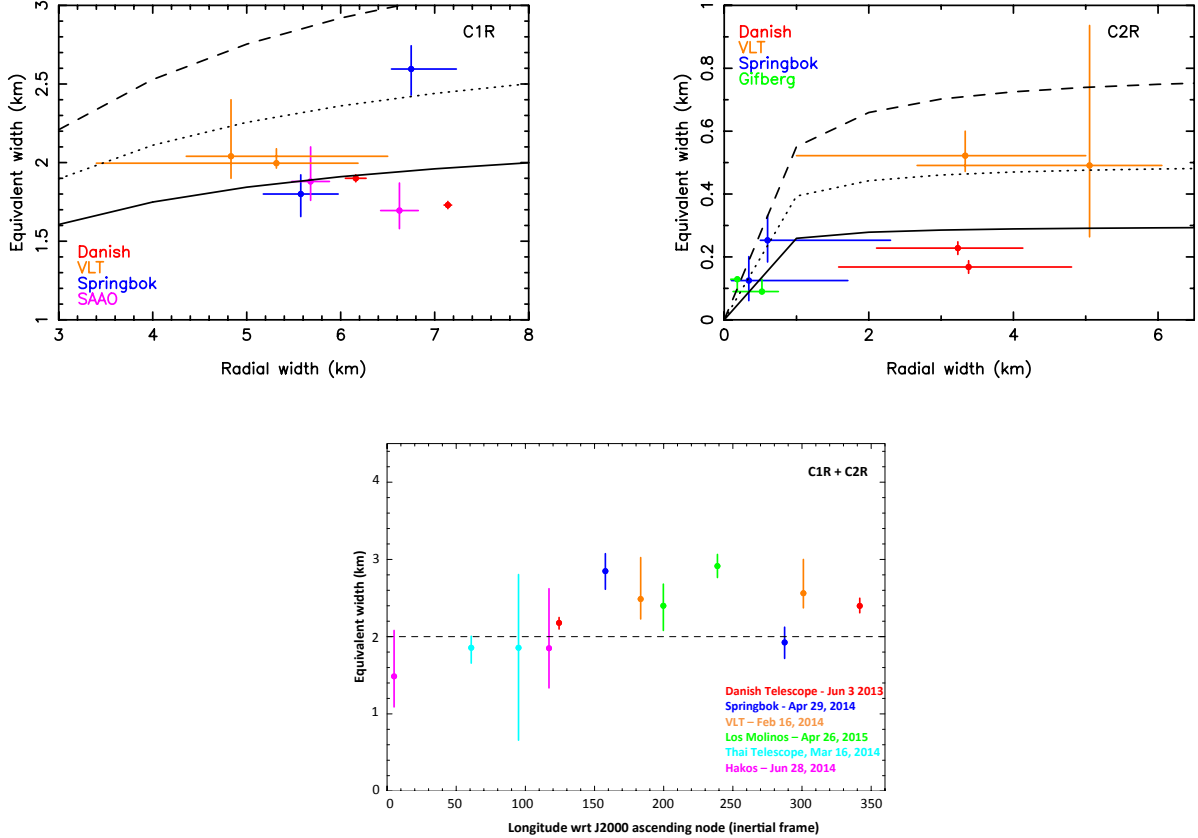
Fig. 11.— *Top left:* Equivalent width E_p (using Eq. A3) of C1R versus the radial width for resolved events. For information, theoretical lines E_p vs W_r expected from a polylayer ring, see Eq 3, have been plotted in black: with $\bar{A}_\tau = 1.15$ km (solid line), $\bar{A}_\tau = 1.5$ km (dotted line), $\bar{A}_\tau = 2.$ km (dashed line). *Top right*: Same for C2R. The black lines are now with $\bar{A}_\tau = 0.15$ km (solid line), $\bar{A}_\tau = 0.25$ km (dotted line), $\bar{A}_\tau = 0.40$ km (dashed line). *Bottom*: the integrated equivalent width $E_p(1+2)$ of C1R and C2R versus the true longitude L, counted from the J2000 ring plane ascending node, from our best events (resolved or not). As SAAO detected only a C1R occultation, and Gifberg only a C2R event, they have been removed from the plot. The dashed line indicates the mean value of the data points.
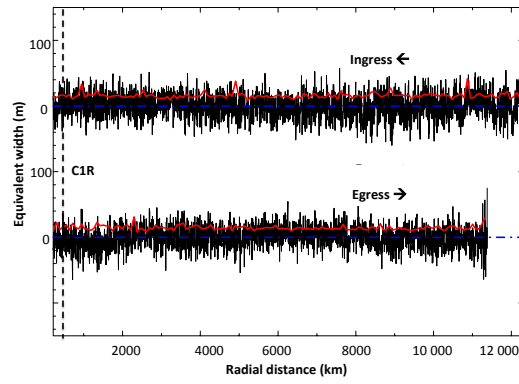
Fig. 12.— Search for faint ring material using the Danish light curve (June 3, 2013 event). Black solid lines: the equivalent width E_p of possible ring material (Eq. 2) vs. the radial distance (in the ring plane) to Chariklo's center. The data points corresponding to the detections of the main body and C1R and C2R have been removed for clarity (for comparison $E_{p,C1R} \sim 2$ km and $E_{p,C2R} \sim 500$ m - see Table 4). The black vertical dotted line indicates the location of C1R, and the horizontal dash-dotted blue lines mark the zero level for E_p. Red solid lines: standard deviation (1σ level) of $E_p(i)$ estimated in bins of width 60 km, see text for details.